Injective Programmable Proanthocyanidin-Coordinated Zinc-Based Composite Hydrogel for Infected Bone Repair

*Yue Wang, Yitao Zhao, Shiyuan Ma, Meimei Fu, Min Wu, Jintao Li, Keke Wu, Xiuli Zhuang, Zhihui Lu, and Jinshan Guo**

Effectively integrating infection control and osteogenesis to promote infected bone repair is challenging. Herein, injective programmable proanthocyanidin (PC)-coordinated zinc-based composite hydrogels (ipPZCHs) are developed by compositing antimicrobial and antioxidant PC-coordinated zinc oxide (ZnO) microspheres with thioether-grafted sodium alginate (TSA), followed by calcium chloride ($CaCl_2$) crosslinking. Responsive to the high endogenous reactive oxygen species (ROS) microenvironment in infected bone defects, the hydrophilicity of TSA can be significantly improved, to trigger the disintegration of ipPZCHs and the fast release of PC-coordinated ZnOs. This together with the easily dissociable PC-Zn^{2+} coordination induced fast release of antimicrobial zinc (Zn^{2+}) with/without silver (Ag^+) ions from PC-coordinated ZnOs (for Zn^{2+}, > 100 times that of pure ZnO) guarantees the strong antimicrobial activity of ipPZCHs. The exogenous ROS generated by ZnO and silver nanoparticles during the antimicrobial process further speeds up the disintegration of ipPZCHs, augmenting the antimicrobial efficacy. At the same time, ROS-responsive degradation/disintegration of ipPZCHs vacates space for bone ingrowth. The concurrently released strong antioxidant PC scavenges excess ROS thus enhances the immunomodulatory (in promoting the anti-inflammatory phenotype (M2) polarization of macrophages) and osteoinductive properties of Zn^{2+}, thus the infected bone repair is effectively promoted via the aforementioned programmable and self-adaptive processes.

1. Introduction

With infection rates of 1–2% for closed fractures and up to 42.9% for Gustilo-Anderson type-IIIB open fractures,[1–3] bone infection remains the most severe and devastating risk associated with orthopedic implants,[4–6] often leading to implantation failure, amputation and even endangering patients' lives. Moreover, with the harborage by foreign implants, very few bacteria (100–1000 colony forming unites) may induce infection,[5] biofilm formation further elevates antimicrobial difficulty, and bacteria were reported can even invade inside osteoblasts and remain dormant to evade host immune attack,[7] causing infection recurrence (≈40%) and chronic infection.[8] The therapeutic efficacy of clinical bone infection treatment, involving debridement and local/systemic antibiotic administration,[3,9] is unsatisfactory due to early burst antibiotic release, possible antibiotics destroy during the exothermic setting process of antibiotic-loaded acrylic cement, and risk of bacterial resistance.[3] Although lysostaphin and bone morphogenetic protein-2 laden hydrogels,[1,6] antibacterial and osteoinductive sterosomes,[10] orthopedic implants surface functionalized with contact-killing,[11] antifouling[12] or

---

Y. Wang, Y. Zhao, S. Ma, M. Fu, M. Wu, J. Li, K. Wu, Z. Lu, J. Guo
Department of Histology and Embryology
NMPA Key Laboratory for Safety Evaluation of Cosmetics
School of Basic Medical Sciences
Guangzhou 510515, P. R. China
E-mail: jsguo4127@smu.edu.cn

Y. Wang, Y. Zhao, S. Ma, M. Fu, M. Wu, J. Li, K. Wu, Z. Lu, J. Guo
Guangdong Provincial Key Laboratory of Bone and Joint Degeneration Diseases
The Third Affiliated Hospital of Southern Medical University
Southern Medical University
Guangzhou 510630, P. R. China

X. Zhuang
Key Laboratory of Polymer Ecomaterials
Changchun Institute of Applied Chemistry
Chinese Academy of Sciences
5625 Renmin Street, Changchun 130022, P. R. China

Z. Lu, J. Guo
Regenerative Medicine and Tissue Repair Material Research Center
Huangpu Institute of Materials
88 Yonglong Avenue of Xinlong Town, Guangzhou 511363, P. R. China

J. Guo
Guangzhou New Materials Science Center, Changchun Institute of Applied Chemistry
Chinese Academy of Sciences
88 Yonglong Avenue of Xinlong Town, Guangzhou 511361, P. R. China

The ORCID identification number(s) for the author(s) of this article can be found under https://doi.org/10.1002/adhm.202302690

DOI: 10.1002/adhm.202302690

biocide-releasing[13–15] moieties could combat bone infection and promote osteogenesis synchronously in certain extent, these systems are still limited by poor stability, short life-time, bacterial resistance or poor tissue integration. On the other hand, the high reactive oxygen species (ROS) microenvironment[3,16] and highly concentrated local acidic metabolites caused by infection activates osteoclasts and deactivates osteoblasts, resulting in osteonecrosis. Complete removal of infection source is often needed before bone reconstruction;[3,8] the antibacterial and osteogenic processes are always contradictory with each other in traditional strategies,[6,16,17] greatly postpones bone regeneration. A smart strategy effectively integrating infection control and osteogenesis is urgently needed.

Recently, a series of biomaterials with endogenous stimuli (such as pH,[4,18–25] redox,[25–27] enzyme,[25,28,29] and hypoxia[22,25])-responsive antimicrobial ability had been developed, which can transform physical/chemical characteristics and exhibit enhanced or on-demand activated antimicrobial activity leveraging the specific infection-induced microenvironment.[3,16] Compared with conventional antimicrobial agents and biomaterials with responsive antimicrobial ability triggered by exogenous factors such as light, temperature, ultrasound and magnetism,[30–34] the antimicrobial ability of endogenous stimuli-responsive antimicrobial biomaterials could be augmented in the infected sites, and the side effects to normal tissues could also be minimized.[25] Although promising, some of these strategies employed antibiotics thus still have the risk of drug resistance, and most of them did not consider osteogenic property.

With broad antimicrobial spectra, favorable heat resistance and less drug resistance, antimicrobial metallic or inorganic elements, such as silver (Ag), cobalt (Co), copper (Cu), zinc (Zn) and phosphorus (P), had attracted intensive research attention in recent years.[13,16,35–39] Among them, Zn is an essential trace metal element in human body mainly locates in skin and skeletal system, plasma Zn concentration was reported positively correlated with bone mineral density (BMD).[40,41] It is proved that Zn possesses favorable osteoconductivity and osteoinductivity[16,42,43] as well as considerable immunomodulatory function in promoting M2 (anti-inflammatory phenotype) polarization of macrophages.[16,44] As a common Zn donor, zinc oxide (ZnO) exhibits inherent broad antimicrobial activities and is generally recognized as safe by the Food and Drug Administration of the United States.[45] However, the antimicrobial activity of ZnO is believed mostly derived from its ROS productivity,[46] which would also cause damage to surrounding tissues. Moreover, the release rate of osteogenic Zn^{2+} from ZnO is very slow,[16,45,46] most zinc-based orthopedic biomaterial design also did not consider the adaptivity to the endogenous infection-induced microenvironments, greatly limited their application in infected bone therapy.

As a typical plant-derived polyphenol, proanthocyanidin(s) (PC) is listed as one of the most effective antioxidants[47] and can inhibit the attachment of inflammatory cells,[48] thus becomes increasingly attractive in biomaterial designs to combat oxidant stress and modulate high ROS and inflammatory microenvironment.[13,48–50] Cranberry proanthocyanidin was also reported can rescue antibiotic efficacy by interfering the intrinsic antibiotic resistance of Gram-negative bacteria.[51] With multiple phenolic and hydroxyl groups, PC is able to coordinate with various metal ions to form metal-phenolic coordination polymers (MPCPs) or metal-phenolic networks (MPNs).[13,50] Herein, via a facile one-pot hydrothermal reaction (in ethanol) of zinc acetate in the presence of PC without or with $AgNO_3$, PC-coordinated ZnO (PC-ZnO) or silver nanoparticles (Ag NPs) modified and PC-coordinated ZnO (Ag-PC-ZnO) is synthesized, which is composited with thioether-grafted sodium alginate (TSA) and further crosslinked by calcium chloride ($CaCl_2$) to give an injective programmable proanthocyanidin-coordinated zinc-based composite hydrogel (ipPZCH) for infected bone repair (**Scheme 1**). The introduction of easily dissociable PC-Zn^{2+} coordination bonds endows PC-ZnO and Ag-PC-ZnO with tremendously improved release rates of both Zn^{2+} and Ag^+ (for Zn^{2+}, all > 100 times that of pure ZnO). The hydrophobic thioether groups are able to be converted into hydrophilic sulfone or sulfoxide groups by ROS, further conferring the hydrogel with ROS scavenging ability and bringing ROS-responsiveness to accelerate the release of antimicrobial PC-ZnO or Ag-PC-ZnO, which, together with the PC-coordination induced fast release of antimicrobial metal ions from PC-ZnO or Ag-PC-ZnO as well as the specific dual metal antimicrobial mechanism, augments the antimicrobial efficacy in infected bone defects. At the same time, the concurrently released PC scavenges endogenous and exogenous (produced during the antimicrobial process) ROS, defensing the surrounding tissues from damage, the strong antioxidant ability providing by PC further improves the immunomodulatory ability of Zn^{2+}, beneficial for the following osteogenesis. The ROS-responsiveness, the antimicrobial ability, the antioxidant, anti-inflammatory, and immunomodulatory functions, the biocompatibility and osteogenic properties of ipPZCHs are thoroughly investigated both in vitro and in vivo. The developed ipPZCHs serve as a programmable platform that not only can greatly amplify the antimicrobial performance leveraging the high ROS microenvironment in the infected bone defect sites and the ROS-responsiveness of the hydrogel, but also can be self-adaptive to clean the smoke of gunpowder, the excess ROS left in the antimicrobial battlefield, paving the way for the sequential osteogenesis to accelerate infected bone repair.

2. Results and Discussion

2.1. Synthesis and Characterizations of Modified ZnO, TSA, and Composite Hydrogels

PC-ZnO and Ag-PC-ZnO were synthesized adapted from the facile "one-pot" hydrothermal reaction of ZnO[52,53] in the presence of PC (without or with $AgNO_3$). The successful introduction of PC in PC-ZnO and Ag-PC-ZnO is confirmed by the appearance of the characteristic peaks of aromatic rings and phenolic hydroxyl groups on PC at 1497 and 1285 cm^{-1} respectively in the Fourier transform infrared (FTIR) spectra (**Figure 1**A). While, the X-ray diffraction (XRD) curve of PC-ZnO shows no difference from that of ZnO (Figure 1B), implying that the inclusion of PC did not transform the crystalline structure of ZnO. The successful inclusion of Ag NPs in Ag-PC-ZnO is also proved by the show up of the characteristic peaks of Ag NPs (38.1, 44.4, and 64.6°)[37] in the XRD curve of Ag-PC-ZnO (Figure 1B). As shown in the thermogravimetric analysis (TGA) curves, although ZnO

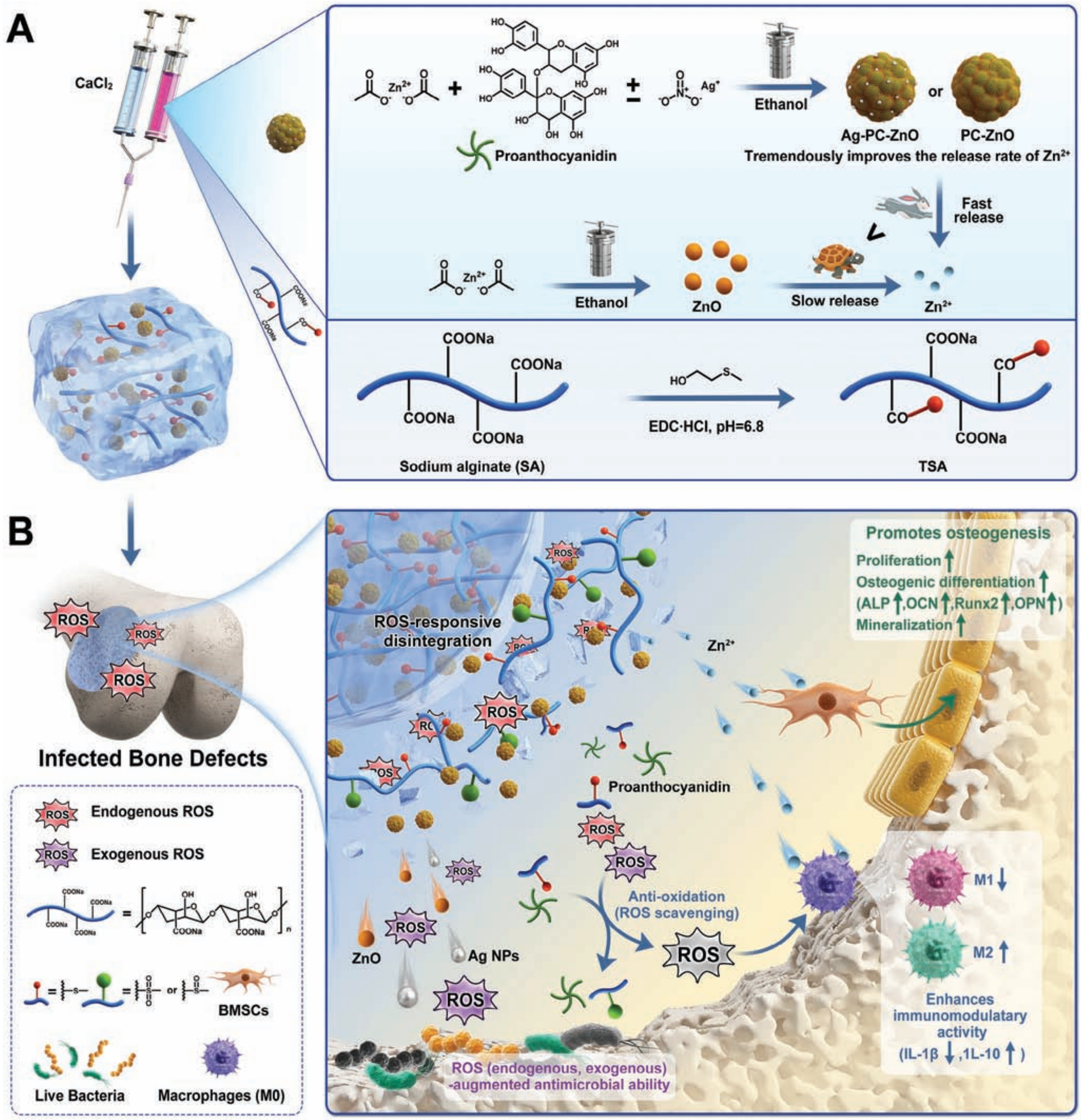

Scheme 1. A) Synthesis of proanthocyanidin (PC)-coordinated ZnO (PC-ZnO) as well as silver nanoparticles (Ag NPs) modified and PC-coordinated ZnO (Ag-PC-ZnO), and the fabrication of injective programmable proanthocyanidin-coordinated zinc-based composite hydrogels (ipPZCHs). B) ipPZCHs exhibit ROS-responsive disintegration behavior, allowing the release of active ingredients to programmably augment antimicrobial ability, provide strong antioxidant activity, enhance immunomodulatory activity, and promote osteogenesis for infected bone repair.

exhibited negligible weight loss (<2.5%) between 25 and 1000 °C under N_2 atmosphere, the weight losses of PC-ZnO and Ag-PC-ZnO reached ≈32.5% and ≈35% respectively (Figure 1C), further confirming the successful inclusion of PC and indicating that PC molecules integrate the internal structure of the modified ZnOs through PC-Zn^{2+} coordination. This can be further proved by the significant morphology change from nanoparticles (<100 nm) for pure ZnO to microspheres for PC-ZnO (≈3 μm) and Ag-PC-ZnO (≈2 μm) (Figure 1D). It is deemed that although the existence of PC-Zn^{2+} coordination bonds in the modified ZnOs did not transform the lattice parameters of the ZnO crystalline, it did dominate the organized aggregation of small ZnO crystals into stacked cauliflower-like microspheres (Figure 1D and Figure S1 in Supporting Information).[54–56] In the case of Ag-PC-ZnO, Ag^+

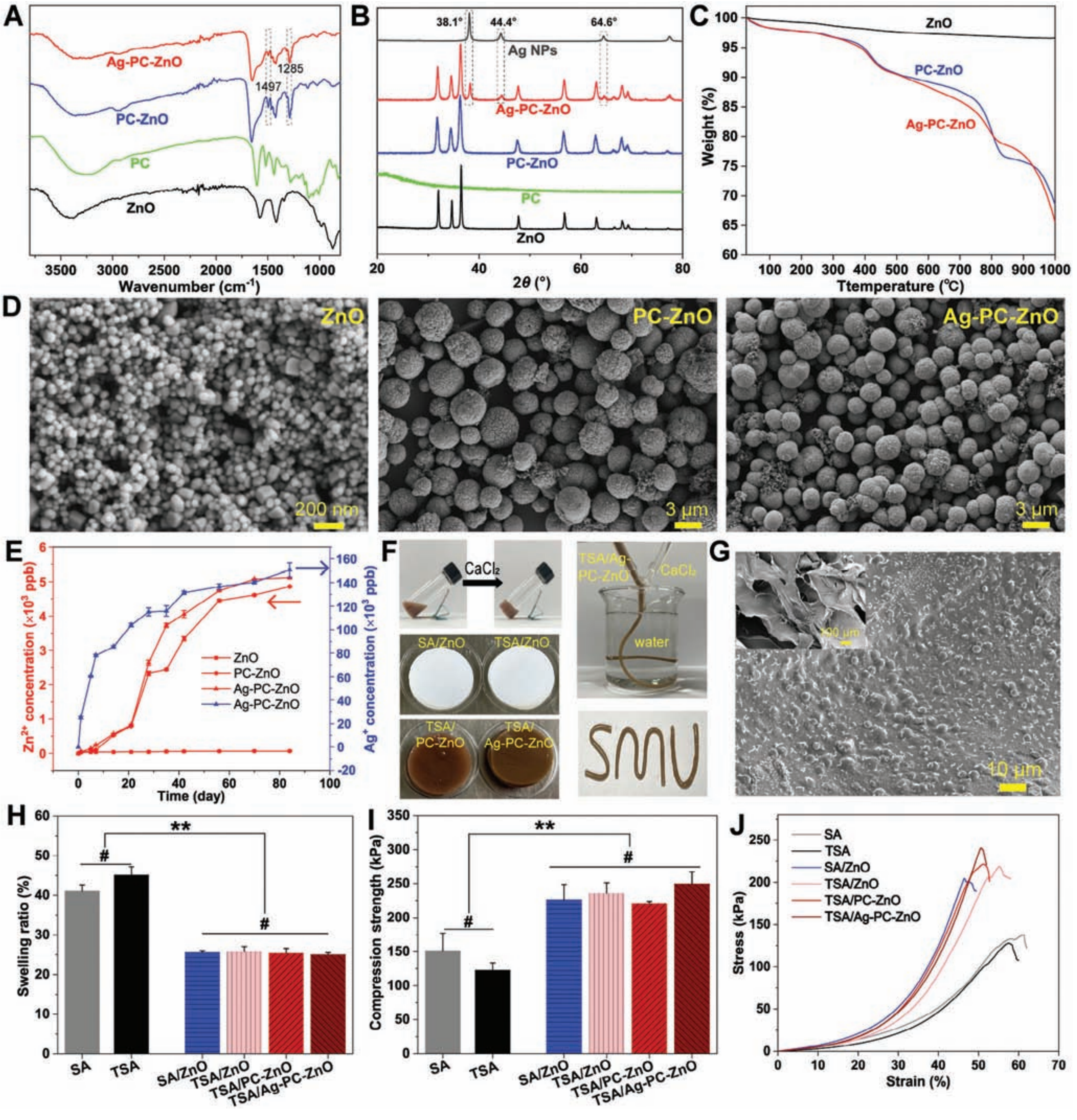

Figure 1. Characterizations of PC-coordinated ZnOs and ipPZCHs: A) FTIR spectra, B) XRD patterns, and C) TGA curves of ZnO, PC-ZnO, and Ag-PC-ZnO. D) SEM images of ZnO, PC-ZnO and Ag-PC-ZnO. E) The Zn^{2+} and Ag^{+} release curves from ZnO, PC-ZnO, and Ag-PC-ZnO ($n = 4$). F) The gelation behavior, general views, and injective behavior of ipPZCHs. G) SEM image of freeze-dried TSA/Ag-PC-ZnO. H) Swelling ratios, I) compression strengths, and J) representative stress–strain curves of different composite hydrogels at wet state ($n = 3$). $^{*}p < 0.05$, $^{**}p < 0.01$, $^{\#}$ represents no significant difference ($p > 0.05$).

is reduced in situ into Ag NPs and a single Ag NP can connect to multiple pyrogallol groups, thus the formation of PC-Zn^{2+} coordination bonds was also affected, resulting in slightly reduced particle size for Ag-PC-ZnO (Figure 1D). The elemental mapping images (Figure S2, Supporting Information) once more confirm the successful introduction and uniform distribution of PC and Ag NPs in the modified ZnOs.

The release of Zn^{2+}, Ag^{+}, and PC from the modified ZnOs in phosphate buffered saline (PBS,pH 7.4) were also monitored by inductively coupled plasma-mass spectrometry (ICP-MS) and

UV–vis spectrometer, respectively. As shown in Figure 1E, the Zn^{2+} release rates significantly increased after PC-coordination, with the accumulative release concentration of Zn^{2+} on the 84th day (14 weeks) being tremendously increased from ≈50 parts per billion (ppb) for pure ZnO to ≈5000 ppb for the modified ZnOs, increased ≈100 times. In our opinion, although the Zn^{2+}-PC coordination did not change the lattice structure of ZnO, the connection mode of ZnO crystals of PC-ZnO or Ag-PC-ZnO was believed different from that of pure ZnO. We conjecture that PC-ZnO or Ag-PC-ZnO microspheres might be composed of both PC-Zn^{2+} complexes and ZnO crystals bridged with PC through PC-Zn^{2+} coordination bonds. And the existence of Zn^{2+}-PC coordination bonds might also increase the surface lattice defects of ZnO crystals. Therefore, a portion of Zn^{2+} could be rapidly released from the PC-coordinated ZnOs, resulting in a significant improvement in the overall release rate of Zn^{2+} from PC-coordinated ZnOs than from pure ZnO. The Ag^+ release rate from Ag-PC-ZnO was even faster than that of Zn^{2+}, with an accumulative release concentration of Ag^+ reached ≈150 parts per million (ppm) on the 84th day (Figure 1E). The release rates of Ag^+ were nearly 30 times of that of Zn^{2+} from Ag-PC-ZnO during the tested time period, which is believed caused by the difference between the material forms of silver and zinc. In Ag-PC-ZnO, Ag^+ is reduced into Ag NPs and a single Ag NP can be connected to multiple pyrogallol groups of PC. The presence of coordination bonds enabled the fast release of Ag NPs from Ag-PC-ZnO in a short period of time, and the released Ag NPs were digested by HNO_3 into Ag^+ and detected by ICP-MS. The introduction of Ag NPs also affects the formation of PC-Zn^{2+} coordination bonds, thus affects the release of Zn^{2+} from Ag-PC-ZnO, the release of Zn^{2+} from Ag-PC-ZnO was slightly faster than that from PC-ZnO (Figure 1E). But the difference of release rates of Zn^{2+} from PC-ZnO and Ag-PC-ZnO was not significant, especially in the beginning 30 d. Additionally, effective release of PC from the modified ZnOs could also be detected, the accumulative release concentrations of PC, calculated according the standard curve shown in Figure S3A in the Supporting Information, reached ≈180 and ≈200 mg L^{-1} for PC-ZnO and Ag-PC-ZnO respectively (Figure S3B, Supporting Information). The fast release of Ag^+ could bring a strong antimicrobial crush, which together with the relatively slower but durable (based on the feeding ratio of Zn/Ag) Zn^{2+} release guarantee effective long-term antimicrobial performance when treating infected bone defects. And the concurrently released PC molecules effectively scavenge ROS, beneficial for protecting the surrounding tissues from damage and promoting the subsequent osteogenesis.

To develop smart composite hydrogels with endogenous stimuli-responsibility, the thioether groups with ROS-responsibility was introduced to the side chains of sodium alginate (SA) to synthesize thioether grafted sodium alginate (TSA, Scheme 1). The successful introduction of thioether group into TSA is confirmed by the appearance of two new peaks at 2.78 and 1.94 ppm in the ^{1}H-NMR spectrum (Figure S4A, Supporting Information), which are assigned to the protons from $-CH_2-S-$ and $-S-CH_3$ of the thioether groups respectives.[27] The grafting ratio of thioether group on TSA was calculated to be ≈9% by ^{1}H-NMR. No significant difference is detected in the FTIR spectra of SA and TSA (Figure S4B, Supporting Information). TSA was then composited with the modified ZnOs and further crosslinked by $CaCl_2$ to give uniform ipPZCHs for infected bone repair (Scheme 1 and Figure 1F). The nomenclature and compositions of different ipPZCH composite hydrogels are shown in Table S1 in the Supporting Information. The injectability of ipPZCHs was well studied, immediate crosslinking could be realized when the composite solution of TSA/Ag-PC-ZnO and $CaCl_2$ was injected and mixed in water and the crosslinked hydrogel could be pushed out from a needle to write the letters Southern Medical University ("SMU") (Figure 1F). As reflected by the scanning electron microscopy (SEM) images of the freeze-dried hydrogels (Figure 1G and Figure S5, Supporting Information), the crosslinked ipPZCHs possess high porosity, and the uniformly distribution of the modified ZnOs in the hydrogels could also be clearly observed. The favorable injectability of ipPZCHs guarantees their adaptability to irregular bone defects, and the high porosity of the hydrogels facilitates cell ingrowth and nutrient penetration, all beneficial for bone regeneration.

To further study the applicability of ipPZCHs, their swelling ratios and mechanical properties were thoroughly investigated. As shown in Figure 1H, comparing with pure organic hydrogels of SA (41.0% ± 1.56%) and TSA (45.0% ± 2.10%), the swelling ratios of the composite hydrogels (percentage of ZnO or modified ZnO = 30 wt%) significantly decreased to ≈25% ($p < 0.01$), and there is no significant difference between different composite hydrogels. Although the inclusion of ZnO or modified ZnOs does not significantly increase the initial moduli and peak strains of the composite hydrogels, the compression strengths of them (≈225 kPa) are significantly higher than that of SA and TSA hydrogels (≈125 kPa) (Figure 1I and Figure S6, Supporting Information). This stress-induced reinforcement feature of the composite hydrogels can also be clearly reflected in the representative stress–strain curves shown in Figure 1J, which is believed closely related to the inclusion of inorganic filler in the hydrogels. This can also be clearly seen from the result that the increase of Ag-PC-ZnO contents in TSA/Ag-PC-ZnO composite hydrogels increases the compression strengths and moduli (Figure S7, Supporting Information). However, higher content of modified ZnO might also bring toxicity concerns, thus the composite hydrogels with 30 wt% ZnO/modified ZnO were chosen for the following studies.

2.2. The In Vitro Antioxidant Properties of the Modified ZnOs and Composite Hydrogels

The high endogenous ROS microenvironment created by bacterial infection is one of the main reasons causing osteonecrosis in the infected bone defect sites,[3] which together with the exogenous ROS produced during the antimicrobial process,[46] need to be scavenged, to proceed the subsequential bone regeneration. Being listed as one of the most effective antioxidants,[47] PC is expected can confer the PC-coordinated ZnOs with considerable antioxidant activity, and the thioether groups on TSA should also possess certain antioxidant ability by chemically reacting with H_2O_2.[27] The in vitro antioxidant properties of the modified ZnOs and composite hydrogels were evaluated using 1,1-diphenyl-2-trinitrophenylhydrazine (DPPH) assay[19,30] and H_2O_2 scavenging assay.[57,58] As shown in Figure S8A,B in the Supporting Information, after 3 mL DPPH solution

(0.1 mmol L^{-1}) being treated with 3.0 mg pure ZnO for 5 min, the absorbance of the remaining DPPH was nearly the same as that of the control, showing negligible antioxidant activity (DPPH scavenging percentage = 1.7% ± 1.67%). While, PC-coordinated ZnOs all exhibited strong antioxidant ability as expected, with DPPH scavenging percentages at 75.8% ± 0.39% and 73.0% ± 0.21% respectively after 5 min treatment, and further prolonging the treating time to 10 min leading to a DPPH scavenging percentage as high as 94.8% ± 1.18% for Ag-PC-ZnO (Figure S8C,D, Supporting Information). The inclusion of ROS-producing Ag NPs has insignificant impact to the strong antioxidant activity of Ag-PC-ZnO. Although TSA showed weak and only slightly higher DPPH scavenging percentage (7.4% ± 0.96%) than that of SA (4.9% ± 0.07%) after the same treating time of 20 min (**Figure 2**A,B), the remaining H_2O_2 concentration was tremendously reduced to 33.8% ± 0.59% after being treated with TSA for only 10 min, significantly lower than that of SA (75.5% ± 2.23%, Figure 2C), demonstrating considerable antioxidant activity of TSA. Along with the extension of treating time by TSA, the remaining H_2O_2 concentration continuously decreased, with the final H_2O_2 concentration < 20% after 6 h (Figure 2C). The non-negligible H_2O_2 elimination ability of pure SA hydrogel might be attributed to the reducibility of mannuronate and guluronate rings in SA,[59] which can be oxidized into aldehyde groups by H_2O_2. Comparing with SA/ZnO and TSA/ZnO which showed very weak DPPH scavenging ability (scavenging percentage < 7% after 5 min), the DPPH scavenging percentages of both TSA/PC-ZnO (45.5% ± 0.32%) and TSA/Ag-PC-ZnO (40.4% ± 3.54%) were significantly higher (Figure 2A,B). Although TSA showed much better H_2O_2 elimination ability (Figure 2C), the H_2O_2 elimination activities of SA/ZnO and TSA/ZnO were nearly the same (Figure 2D), which is believed caused by the strong ROS (including H_2O_2)-producing ability of ZnO in water. While, benefiting from the strong antioxidant ability of PC, the remaining H_2O_2 concentration was greatly reduced to 38.2% ± 0.59% and 45.1% ± 0.90% of its original level within 10 min, and all ≈ 20% after 3 h (Figure 2D). These results preliminarily proved the antioxidant activity of both PC-coordinated ZnOs (PC-ZnO and Ag-PC-ZnO), TSA and the composite hydrogels.

Moreover, the intracellular ROS scavenging capability of TSA and the composite hydrogels was further evaluated by coculturing them with rat bone-marrow mesenchymal stem cells (rBMSCs) which were stimulated by H_2O_2 to achieve excessive intracellular ROS.[60,61] As shown in Figure 2E and Figure S9 in the Supporting Information, the fluorescence intensity, reflecting intracellular ROS concentration, of the TSA+H_2O_2 group (138.7% ± 3.39%) was significantly ($p < 0.05$) lower than that of the H_2O_2 and SA+H_2O_2 groups (intensities nearly the same, all ≈160%), once again confirming the antioxidant activity of TSA. However, the fluorescence intensities of the SA/ZnO (171.8% ± 6.14%) and TSA/ZnO (165.1% ± 4.23%) groups were even higher than that of the H_2O_2 group, indicating that pure ZnO could increase the intracellular oxidative stress and exceed the antioxidant ability of TSA (Figure 2E and Figure S9, Supporting Information). While, the fluorescence intensities of the TSA/PC-ZnO (120.2% ± 4.13%) and TSA/Ag-PC-ZnO (122.1% ± 4.20%) groups significantly decreased again, became even lower than that of the TSA+H_2O_2 group (Figure 2E and Figure S9, Supporting Information). The flow cytometry results (Figure 2F) exhibited the same trend. These results further confirmed the considerable antioxidant activity of TSA and PC-coordinated ZnOs, and demonstrate that PC-coordinated ZnOs can suppress the oxidative stress productivity of ZnO and successfully rescue the high ROS microenvironment, well agreeing with previous H_2O_2 scavenging assay results (Figure 2C,D).

Furthermore, the effect of TSA and the composite hydrogels to the activities of intracellular antioxidant enzymes, including superoxide dismutase (SOD), catalase (CAT), and glutathione peroxidase (GPx), was also studied using rBMSCs.[30,58,62] As shown in Figure 2G–I, both the activities of SOD and GPx of the TSA sample (136.2% ± 8.50% and 198.4% ± 8.45% respectively) were significantly higher than that of the control and SA (99.9% ± 3.97% and 155.8% ± 5.98% respectively) groups. The CAT activity of the TSA group (110.2% ± 3.35%) was also slightly higher comparing with the control (100.0% ± 6.06%) and SA (102.5% ± 1.93%) groups. Inclusion of ZnO in the hydrogel (SA/ZnO and TSA/ZnO) decreased the antioxidant enzyme activity comparing with that of SA and TSA. In the case of CAT, the activities of SA/ZnO (80.3% ± 3.60%) and TSA/ZnO (93.2% ± 7.96%) groups were even significantly lower than the control group (Figure 2G–I). While, the inclusion of PC-ZnO in the hydrogel significantly elevated the activities of SOD, CAT, and GPx to 183.7% ± 5.50%, 143.3% ± 3.68%, and 224.9% ± 9.26% of the original levels respectively, and further inclusion of Ag NPs (TSA/Ag-PC-ZnO) only brought insignificant decrease of the antioxidant enzymes' activities comparing to that of TSA/PC-ZnO. These results suggest that there is a vital link between exogenous antioxidants and endogenous antioxidant enzymes and they work coordinately. All the above results reveal that ipPZCHs not only possess improved ROS scavenging ability derived from both PC and the thioether groups on TSA but also can activate the endogenous antioxidant defense systems, to provide favorable antioxidant capability and to rescue the side effect brought by ROS-productive ZnO.

2.3. ROS-Responsibility and Antimicrobial Properties of ipPZCH Composite Hydrogels

ROS-responsive ipPZCHs are expected can response to the high endogenous ROS microenvironment, to disintegrate and release antimicrobial PC-ZnO or Ag-PC-ZnO, and the exogenous ROS produced by these antimicrobial agents during the antimicrobial process would further accelerate the disintegration of ipPZCHs, thus the antimicrobial efficacy of ipPZCHs in infected bone defects can be augmented (**Figure 3**A). First, the ROS-responsibility of the composite hydrogels is studied by observing the change of the composite hydrogels in H_2O_2 containing PBS, using TSA/Ag-PC-ZnO as the representative composite hydrogel and SA/Ag-PC-ZnO as control. It can be seen from Figure 3B, after being immersed in H_2O_2 containing PBS for 3 d, TSA/Ag-PC-ZnO remarkably swelled and started to disintegrate, and almost complete disintegration was observed after 5 d. While, only swelling can be observed after TSA/Ag-PC-ZnO being immersed in PBS for 5 d, and no visible disintegration or even swelling was observed for SA/Ag-PC-ZnO in either PBS or H_2O_2 containing PBS, indicating the critical role of thioether modification of SA in the ROS-responsibility (Figure 3B). This can be further proved by the ROS-accelerated degradation behavior of

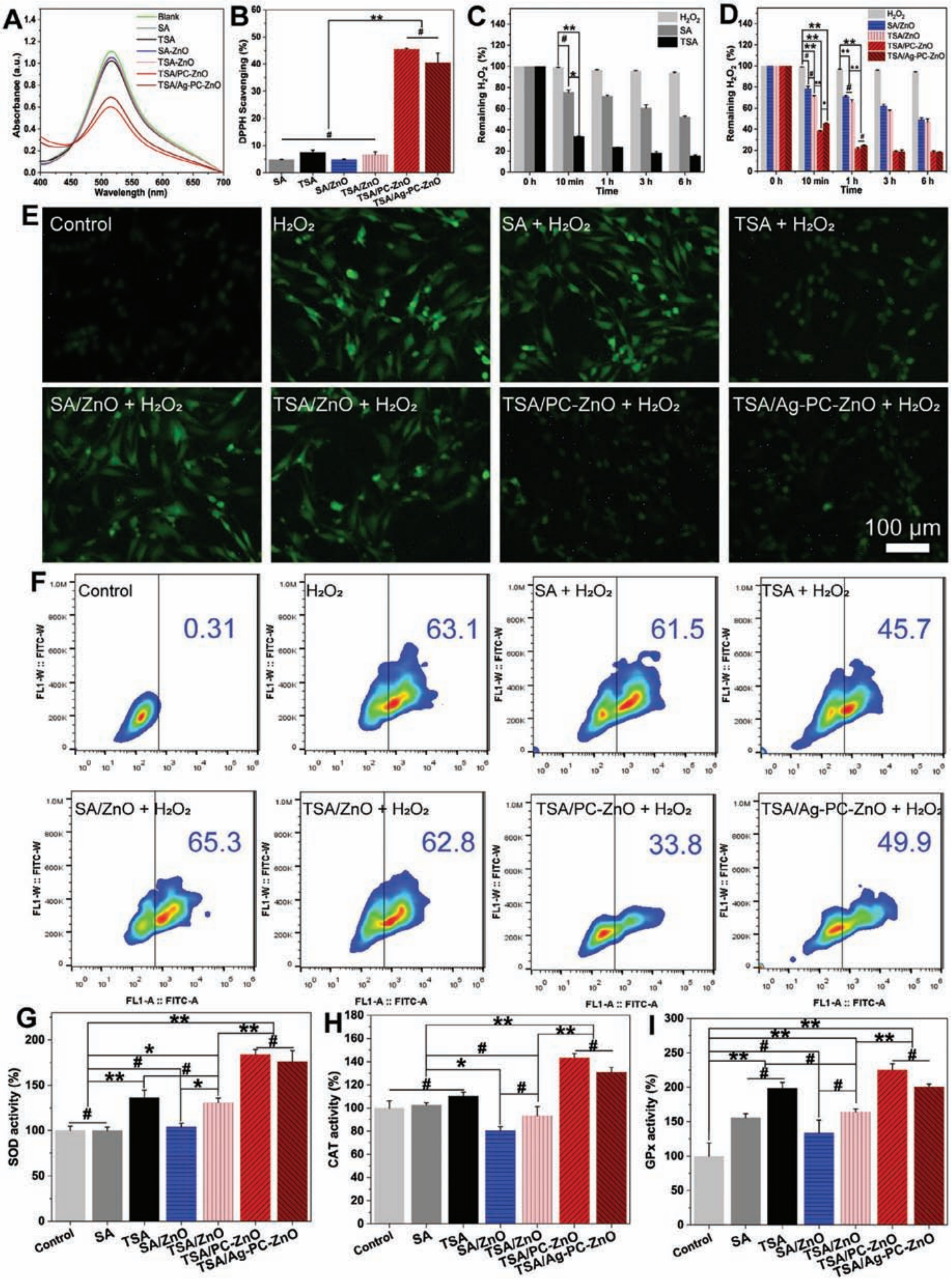

Figure 2. Antioxidant activity of ipPZCHs: A) UV–vis spectra and B) the corresponding DPPH scavenging percentages of different composite hydrogels after incubating for 20 min. Remaining H_2O_2 (%) after being treated with C) SA, TSA and D) composite hydrogels for different times ($n = 3$). E) The fluorescence images and F) flow cytometry quantification results reflecting intracellular ROS levels of rBMSCs after being treated with different composite hydrogels. The activities of intracellular antioxidant enzymes in rBMSCs including G) SOD, H) CAT, and I) GPx after being treated with different composite hydrogels ($n = 3$). $^{*}p < 0.05$, $^{**}p < 0.01$, $^{\#}$ represents no significant difference ($p > 0.05$).

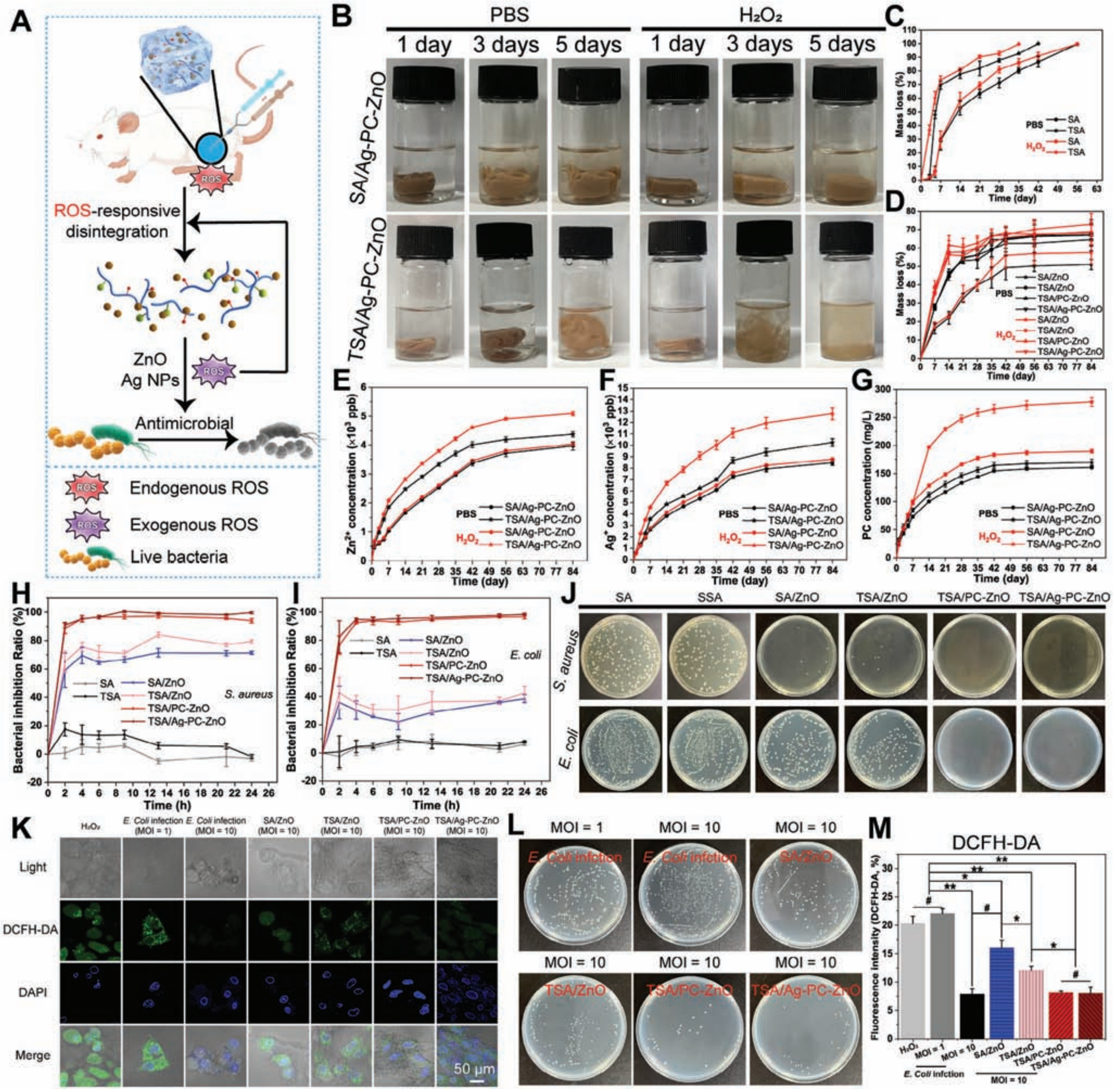

Figure 3. ROS-responsive and the antimicrobial properties of ipPZCHs: A) schematic diagram, B) photos of SA/Ag-PC-ZnO and TSA/Ag-PC-ZnO composite hydrogels immersed in PBS or H_2O_2 (2.0 mм) containing PBS for different times. Mass losses of C) SA, TSA and D) composite hydrogels, release curves of E) Zn^{2+}, F) Ag^{+}, and G) PC from SA/Ag-PC-ZnO and TSA/Ag-PC-ZnO when immersed in PBS or H_2O_2 (2.0 mм) containing PBS ($n = 3$). The antibacterial kinetics curves of different composite hydrogels against H) *S. aureus* and I) *E. coli*, and J) representative images of bacteria colonies grown on agar plates for different samples after incubation for 24 h ($n = 3$). K) Fluorescent images of *E. coli* infected cells at a multiplicity of infection (MOI, bacteria/cells) = 1 or 10, L) image of the residual bacteria colonies of lysed cells casted on agar plates, and M) the fluorescence semi-quantification results of reactive oxygen species (ROS) of different samples ($n = 3$). $^{*}p < 0.05$, $^{**}p < 0.01$, $^{\#}$ represents no significant difference ($p > 0.05$).

TSA (Figure 3C). This is derived from the change of the hydrophobic thioether groups on TSA into hydrophilic sulfone or sulfoxide groups triggered by ROS, as proven by the show up of a new peak at 2.8–3.2 ppm in the ^{1}H-NMR of TSA after being treated by H_2O_2 (TSA+H_2O_2) (Figure S10, Supporting Information).[27] As shown in the degradation profiles of the composite hydrogels (Figure 3D), the degradation rates of SA/ZnO were significantly lower than that of TSA/ZnO, TSA/PC-ZnO, and TSA/Ag-PC-ZnO, in either PBS, this might be caused by that thioether grafting on SA reduces the density of $—COO^{-}—Ca^{2+}—^{-}OOC—$ ion crosslinking sites. As expected, the ROS-responsibility of TSA also accelerated the degradation of TSA/PC-ZnO and TSA/Ag-PC-ZnO in H_2O_2 containing PBS, especially in the beginning 40 d: for example, the mass losses of

TSA/Ag-PC-ZnO degrading in H_2O_2 containing PBS for 7 and 14 d were 35.1% ± 3.36% and 56.2% ± 2.82%, respectively, significantly higher than that of TSA/Ag-PC-ZnO degrading in PBS for 7 (27.7% ± 1.47%) and 14 (46.5% ± 0.68%) days (Figure 3D).

Moreover, the effect of ROS-responsibility of ipPZCHs to the release of metal ions (Zn^{2+} and Ag^+) and PC were also investigated using TSA/Ag-PC-ZnO as the representative, with SA/Ag-PC-ZnO serving as control. As shown in Figure 3E,F, the release rates of both Zn^{2+} and Ag^+ from SA/Ag-PC-ZnO in PBS and H_2O_2 containing PBS showed no obvious difference; but the release of these two metal ions from TSA/Ag-PC-ZnO in H_2O_2 containing PBS were significantly faster than in PBS (Figure 3E,F). The accumulative release concentrations for Zn^{2+} and Ag^+ from TSA/Ag-PC-ZnO in H_2O_2 containing PBS on the 84th day were at 5093.3 ± 78.46 and 12 769.0 ± 521.37 ppb respectively, significantly higher than that in PBS on the same time point (4376.7 ± 92.86 ppb for Zn^{2+}, 10 250.5 ± 323.36 ppb for Ag^+). Interestingly, the release rates of PC from both SA/Ag-PC-ZnO and TSA/Ag-PC-ZnO in H_2O_2 containing PBS were significantly higher than the PC release rates of them in PBS (Figure 3G), indicating that except for thioether groups, PC, as a kind of polyphenol, might also possess ROS responsibility. This might be the reason that when immersing in H_2O_2 containing PBS, the PC release rates were nearly doubled comparing with that in PBS at the later stage (Figure 3G), with the accumulative release concentration of PC on the 84th day at 277.5 ± 7.76 mg L^{-1} in H_2O_2 containing PBS and 170.0 ± 5.53 mg L^{-1} in PBS. The favorable ROS responsibility of ipPZCHs perfectly accommodates to the high endogenous ROS microenvironment in infected bone defect sites, leading to accelerated composite hydrogels disintegration thus speeds up the release of the antimicrobial modified ZnOs, which, accompany with PC-Zn^{2+} coordination induced fast release of Zn^{2+} and Ag^+ from the modified ZnOs, enhances the antimicrobial ability of ipPZCHs. High ROS microenvironment was proven can also accelerate the release of PC from TSA/Ag-PC-ZnO, beneficial for the scavenge of the excess endogenous and exogenous ROS, paving the way for the subsequent osteogenesis.

The antimicrobial properties of the modified ZnOs and ROS-responsive ipPZCHs were assessed using *Staphylococcus aureus* (*S. aureus*) and *Escherichia coli* (*E. coli*) as representative Gram-positive and Gram-negative bacteria, respectively. First, the minimal inhibitory concentrations (MICs) of the modified ZnOs were determined using an agar dilution method.[16,37] As shown in Figure S11A,C in the Supporting Information, ZnO, PC-ZnO, and Ag-PC-ZnO all showed strong antibacterial activity against *S. aureus*, with the same MIC of 0.15 625 mg mL^{-1}. While, the antimicrobial ability of ZnO, PC-ZnO, and Ag-PC-ZnO against *E. coli* were much weaker than against *S. aureus*, with MICs of 0.625, 0.625, and 0.3125 mg mL^{-1} respectively (Figure S11A,C, Supporting Information). These results confirm the strong antimicrobial activity of the modified ZnOs, especially for Ag-PC-ZnO and against *S. aureus*, which is deemed derived from the faster release of antimicrobial ions from the modified ZnOs than from pure ZnO, and the application of the Zn and Ag dual-metal antimicrobial mechanism. Moreover, the antimicrobial activity of the ipPZCH composite hydrogels was further evaluated by directly exploring 0.1 g dry hydrogel to 10 mL bacterial suspensions (100× diluted from bacteria suspensions with an optical density (OD) = 0.1), the bacterial inhibition ratios at each preset time points from 0 to 24 h were measured, and the final bacterial suspensions (24 h) were also diluted and casted on agar plates and allowed to grow for 24 h. As shown in Figure 3H,I, for all samples, the bacterial inhibition ratios increased in the initial 4 h and then stabilized at a plateau during the whole 24 h testing period. Pure SA hydrogel showed negligible antimicrobial activity against both *S. aureus* and *E. coli*, and TSA hydrogel only exhibited weak antimicrobial ability against *S. aureus* (bacterial inhibition ratio ≈ 15%) and nearly no antimicrobial ability against *E. coli*. SA/ZnO and TSA/ZnO exhibited only medium antimicrobial activity, with the final bacterial inhibition ratios after 24 h against *S. aureus* at 71.4% ± 1.02% and 79.3% ± 1.23% respectively, and even much lower (38.5% ± 2.70% and 42.4% ± 5.14% for SA/ZnO and TSA/ZnO respectively) against *E. coli* (Figure 3H,I). While, both TSA/PC-ZnO and TSA/Ag-PC-ZnO showed strong antimicrobial ability against both *S. aureus* and *E. coli*, with bacterial inhibition ratios all ≈95% after 4 h (Figure 3H,I), which is believed to be the comprehensive effect of both ROS-induced disintegration of the composite hydrogel and PC-Zn^{2+} coordination induced fast antimicrobial metal ions (Zn^{2+} ± Ag^+). The strong antimicrobial activity of TSA/PC-ZnO and TSA/Ag-PC-ZnO was further confirmed by the bacterial colony growth images shown in Figure 3J.

To mimic the practical application situation that in the infected bone defects, bacterial infection would produce endogenous ROS and affect the surrounding tissue, rBMSCs were cocultured with *E. coli*, and the synchronous antimicrobial and antioxidant activity of the composite hydrogels were studied. As shown in Figure 3K, at an infection level of a multiplicity of infection (MOI, bacteria/cells) = 1, medium bacterial infection was detected (Figure 3L and Figure S12, Supporting Information), possible invasion of bacteria into the cells was found and significant ROS production (Figure 3M) was also observed. The ROS fluorescent morphology was highly similar to the mitochondrial localization, indicating cellular defense mechanism against bacterial infection. While, at an MOI of 10, the cells were severely damaged by a large amount of bacteria (Figure 3K,L and Figure S12, Supporting Information) and exhibited round morphology thus lack of mitochondrial function, resulting in extremely low level of ROS (Figure 3M). When SA/ZnO or TSA/ZnO was applied (MOI = 10), although a large amount of bacteria were killed (Figure 3K2 and Figure S12, Supporting Information), the intracellular ROS level was still high (Figure 3M), which might be attributed to that both the residual bacteria and ZnO would produce ROS. The intracellular ROS level of the TSA/ZnO sample was significantly lower than that of the SA/ZnO one, implying that TSA could scavenge some ROS (Figure 3K). The application of TSA/PC-ZnO and TSA/Ag-PC-ZnO (MOI = 10) not only killed most of the bacteria, but also significantly reduced the intracellular ROS levels (Figure 3K and Figure S12, Supporting Information), once more proving the strong antimicrobial and antioxidant activity of ipPZCHs, well agreeing with previous antioxidant study results (Figure 2). These results further indicate that benefiting from the ROS-responsible TSA as well as the strong antimicrobial and antioxidant activity of PC-coordinated ZnOs, the developed ipPZCHs could effectively kill bacteria and protect the surrounding cells at the same time, well supporting their potential application in infected bone repair.

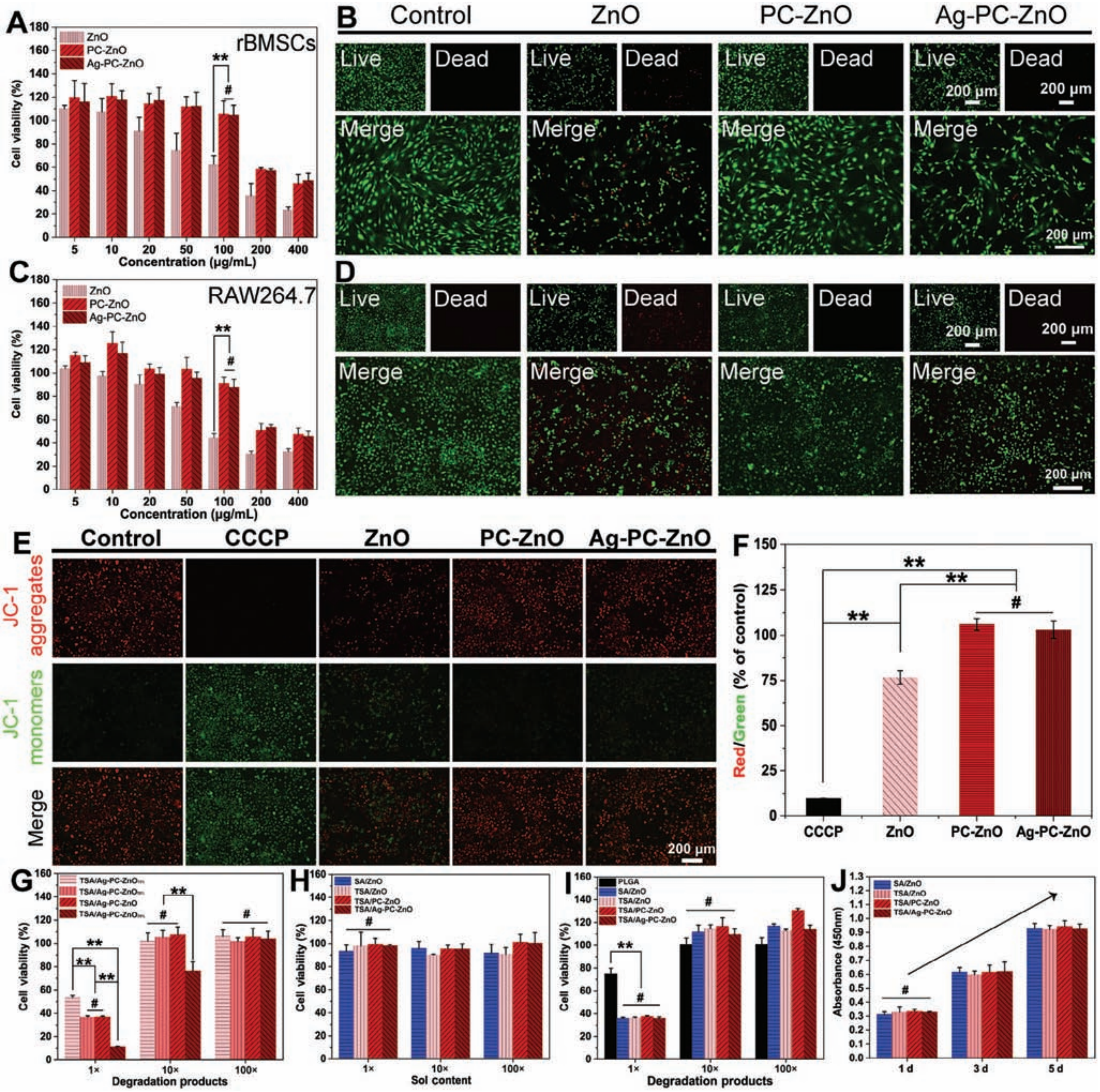

Figure 4. In vitro cytocompatibility of PC-coordinated ZnOs and ipPZCHs: A,C) cell viabilities of PC-coordinated ZnOs with different concentrations and B,D) the corresponding live/dead staining images of cells of different materials (100 μg mL^{-1}) against A,B) rBMSCs and C,D) RAW264.7 cells ($n = 4$). E) The fluorescent images of RAW264.7 cells reflecting mitochondrial membrane potential measured by JC-1 assay and F) the calculated Red/Green ratios ($n = 3$). G) Cell viabilities against rBMSCs for 24 h of the degradation products of TSA/Ag-PC-ZnO$_{x\%}$ ($x = 10$, 20, 30, and 50), H) the sol contents, and I) the degradation products of different composite hydrogels. J) Cell proliferation results of rBMSCs assessed by coculturing with 0.1 mg mL^{-1} TSA/Ag-PC-ZnO for 1, 3, and 5 d ($n = 3$). $^{*}p < 0.05$, $^{**}p < 0.01$, $^{\#}$ represents no significant difference ($p > 0.05$).

2.4. The Cytocompatibility of Modified ZnOs, TSA, and ipPZCH Composite Hydrogels

Favorable biocompatibility of biomaterials is critical for their regenerative medicine applications. The cytocompatibility of the modified ZnOs, TSA, and the composite hydrogels were thoroughly studied using rBMSCs and RAW264.7 (mouse mononuclear macrophage leukemia cells) as cell models (**Figure 4**). As shown in Figure 4A,C, compared with pure ZnO that induces cytotoxicity at very low concentration (>10 μg mL^{-1}), the modified ZnOs show nearly no cytotoxicity at concentrations as high as 100–200 μg mL^{-1}, especially in the case of rBMSCs. This is further proven by the Live/Dead staining images of rBMSCs and RAW264.7 cells after being treated by 100 μg mL^{-1} ZnO or modified ZnO for 24 h (Figure 4B,D). These results preliminarily indicate that PC-coordination greatly improves the cytocompatibility of the modified ZnOs, which can even counteract the toxicity brought by the further introduction of Ag NPs. Moreover, the effect of the modified ZnOs to the apoptosis (reflected by the decrease/loss of mitochondrial membrane potentials, green stained) of RAW264.7 cells was further studied using mitochondrial membrane potential dye (JC-1) staining, and the degree of mitochondrial depolarization was also quantified by the red/green fluorescence intensity ratio.[63] As shown in Figure 4E, the cell mitochondria of the carbonyl cyanide chlorophenylhydrazone (CCCP)-negative group were nearly all stained in green fluorescence, reflecting the loss of mitochondrial membrane potential in this negative control group. For the ZnO group, the amount of surviving cells obviously decreased and a large number of the remaining cells were stained in green fluorescence (with a red/green ratio of 76.6% ± 3.67%), further indicating the strong toxicity of pure ZnO (Figure 4E,F). In contrast, the PC-ZnO and Ag-PC-ZnO groups were dominated by red stained cells, with red/green ratios of 106.0% ± 3.24% and 102.8% ± 4.85% respectively, once more proved the toxicity reducing function of PC (Figure 4E,F). These results also suggest that PC-coordination of ZnO can protect mitochondrial function and reduce apoptosis, beneficial in improving the biocompatibility of the modified ZnOs.

The cytocompatibility of SA and TSA polymers as well as the composite hydrogels (estimated by the soluble (leachable) contents and degradation products) was assessed using cell counting kit-8 (CCK-8) against rBMSCs. Although 10 mg mL^{-1} TSA induced relatively strong cytotoxicity to rBMSCs (cell viability $< 40\%$) comparing to SA (cell viability = 100.8% ± 1.60%) at the same concentration, both TSA and SA exhibited good cytocompatibility (cell viability all around or even $> 100\%$) at concentrations of 1.0 and 0.1 mg mL^{-1} (Figure S13, Supporting Information). From the cytotoxicity results of TSA/Ag-PC-ZnO$_x$ (x representing content of Ag-PC-ZnO, = 10%, 20%, or 50%) and TSA/Ag-PC-ZnO (content of Ag-PC-ZnO = 30%) shown in Figure 4G, it can be seen that higher Ag-PC-ZnO contents led to stronger cytotoxicity, with the cell viability for 1× degradation product of the TSA/Ag-PC-ZnO$_{50\%}$ sample $\approx 10\%$, and still $<80\%$ for its 10× degradation product. While, the degradation products of TSA/Ag-PC-ZnO with 30% Ag-PC-ZnO induced no significant cytotoxicity comparing to Ag-PC-ZnO$_{10\%}$ and Ag-PC-ZnO$_{20\%}$, especially at 10× and 100× (Figure 4G), thus TSA/Ag-PC-ZnO was used for the following studies. The 1× sole contents of SA/ZnO, TSA/ZnO, TSA/PC-ZnO, and TSA/Ag-PC-ZnO all exhibited no cytotoxicity, with the cell viabilities all around or even $>100\%$ (Figure 4H). Although the cell viabilities of the 1× degradation products of SA/ZnO, TSA/ZnO, TSA/PC-ZnO, and TSA/Ag-PC-ZnO all $\approx 30\%$, significantly lower than that of the 1× degradation product of poly(lactic-*co*-glycolic acid) (PLGA) ($\approx 75\%$), the cell viabilities of the degradation products of them at 10× and 100× dilutions all exceeded those of PLGA degradation products at the same dilutions (Figure 4I). The 10× diluted degradation products of all the representing composite hydrogels induced well cell proliferation, with the cell amounts steadily increasing during 1 to 5 d (Figure 4J), which can be also reflected by the live/dead staining results of the 10× diluted degradation product of TSA/Ag-PC-ZnO (Figure S14, Supporting Information). All these results suggest that although thioether grafting on SA and the introduction of ZnO ± Ag NPs brought certain cytotoxicity, both TSA/PC-ZnO and TSA/Ag-PC-ZnO showed acceptable cytocompatibility benefiting from the PC-coordination strategy. The synchronously fast release of PC (especially at high ROS concentration (Figure 3G)) along with Zn^{2+} ± Ag^{+} from PC-coordinated ZnOs, and the oxidation of the thioether groups on TSA could scavenge the ROS produced by antimicrobial ZnO and Ag NPs, thus preserves favorable cytocompatibility for ipPZCHs, paving the way for the sequential osteogenic process.

2.5. The Immunomodulatory and Osteogenic Properties of ipPZCHs

Although inflammatory response is necessary for bone defect repair, excessive inflammatory factors induced by the upregulated pro-inflammatory M1-type macrophages are detrimental to bone regeneration. The experimental results discussed above already reveal that high ROS microenvironment could trigger ipPZCHs' disintegration and the release of PC-coordinated ZnOs (Figure 3), the Zn^{2+} releasing rate from PC-coordinated ZnOs was further tremendously accelerated (> 100 times that of ZnO) due to PC-Zn^{2+} coordination (Figure 1). The accelerated Zn^{2+} release from ipPZCHs is expected can promote osteogenesis benefiting from the favorable immunomodulatory[16,44] and osteoinductive[16] activity of Zn^{2+} and with the help of the antioxidation performance provided by TSA and PC (**Figure 5**A). The immunomodulatory activity of ipPZCHs was assessed by directly exposing RAW264.7 cells to the small pieces or degradation products of TSA/ZnO and TSA/Ag-PC-ZnO in the presence of lipopolysaccharide (LPS) or interleukin-4 (IL-4), with RAW264.7 cells being treated only by LPS or IL-4 to induce M1 or M2 phenotypes as the negative and positive controls respectively. As shown in the flow cytometry results (Figure 5B), both the percentages of M1 (CD206^{-} and CD86^{+}) and M2 (CD206^{+} and CD86^{-}) polarized cells and the M1 M2 ratios of the TSA/ZnO(+LPS/IL-4) samples were nearly the same with that of RAW264.7 cells treated solely by LPS or IL-4, indicating that TSA/ZnO has negligible immunomodulatory effect. This might be attributed to the slow Zn^{2+} release from TSA/ZnO, and the slight antioxidant activity of TSA was attenuated by ROS-producing ZnO. While, TSA/Ag-PC-ZnO hydrogel treatment not only significantly reduced the percentage of LPS-induced M1 polarized cells from 43.5% (treated only by LPS) to 21.6% (TSA/Ag-PC-ZnO+LPS), but also significantly elevated the percentage of IL-4-induced M2 polarized cells from 6.87% (IL-4) to 26.7% (TSA/Ag-PC-ZnO+IL-4) (Figure 5B). And the percentage of M2 polarized cells was further improved to 35.9% when RAW264.7 cells were treated by the 10× degradation product of TSA/Ag-PC-ZnO (Figure 5B), which should be attributed to the higher content of Zn^{2+} in the full degradation product (10× diluted) than in the cell culture medium directly exposing to TSA/Ag-PC-ZnO hydrogel. The favorable immunomodulatory activity of TSA/Ag-PC-ZnO was further confirmed by the immunofluorescence staining images and the semi-quantitative results (Figure 5C–E). The fluorescence intensity of CD86^{+} cells in the TSA/Ag-PC-ZnO+LPS sample (19.9% ± 0.91%) was significantly lower than that of the LPS sample (24.2% ± 1.57%), and the fluorescence intensity of CD206^{+} cells in the

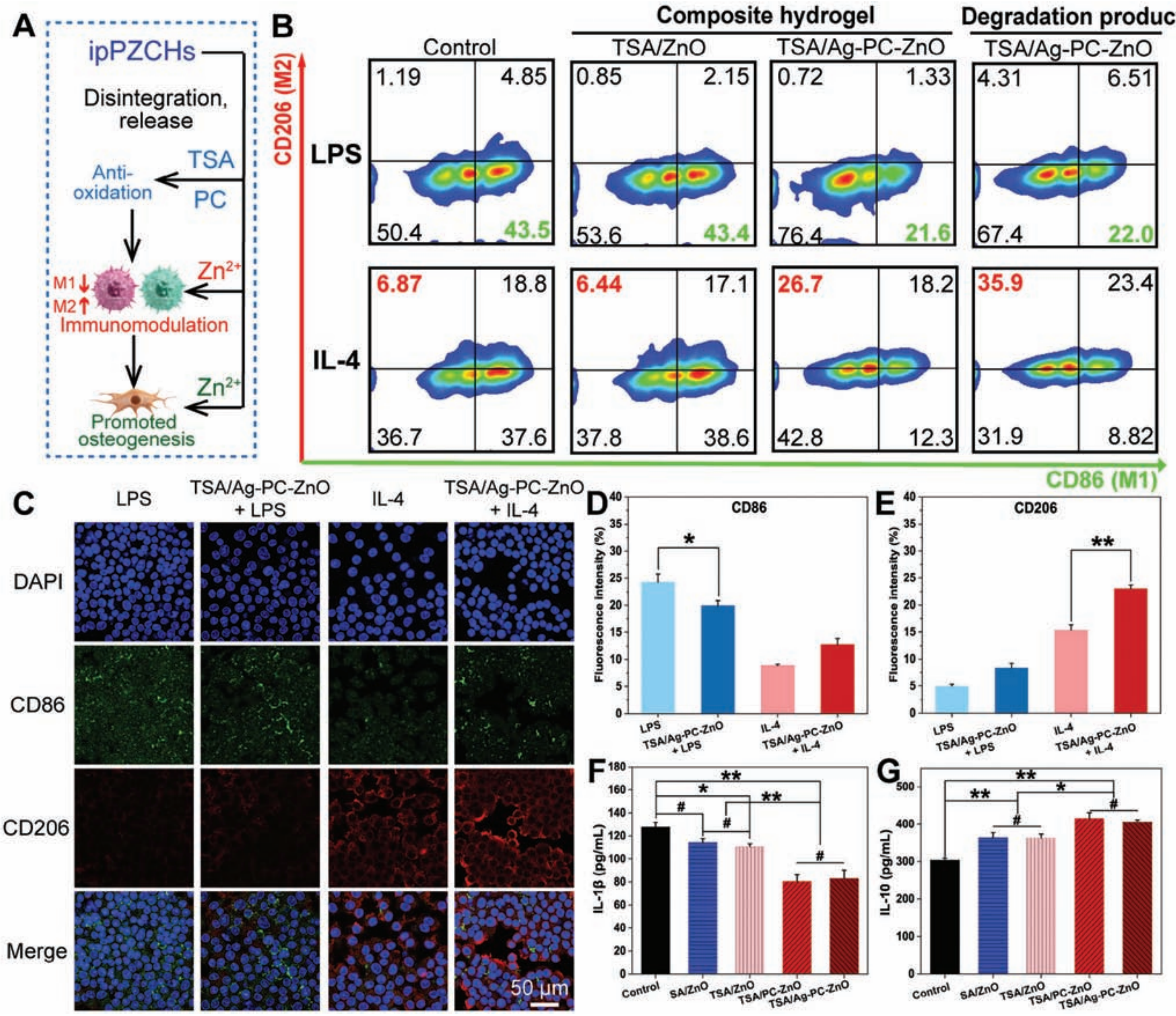

Figure 5. The immunomodulatory and osteogenic properties of ipPZCHs: A) schematic diagram of ipPZCHs' immunomodulatory activity. B) Flow cytometry patterns of RAW 264.7 cells stained with CD206 or CD86 antibody after being treated by different composite hydrogels in the presence of LPS or IL-4. C) Confocal laser scanning microscope (CLSM) images of RAW 264.7 cells stained with CD86 (green), CD206 (red), and 4', 6-diamidino-2-phenylindole (DAPI, blue) after being treated by composite hydrogels in the presence of LPS or IL-4, and the corresponding fluorescent intensities (% area) of D) CD86 and E) CD206, the F) IL-1β and G) IL-10 expression levels obtained by ELISA assay ($n = 3$). *$p < 0.05$, **$p < 0.01$, # represents no significant difference ($p > 0.05$).

TSA/Ag-PC-ZnO+IL-4 sample (23.1% ± 0.64%) was also significantly higher than that of the IL-4 sample (15.3% ± 1.05%). Although the fluorescence intensity of the CD86$^+$ cells in the TSA/Ag-PC-ZnO+IL-4 sample (12.8% ± 1.09%) was higher than that of the IL-4 sample (8.8% ± 0.28%), the ratio of CD206$^+$ cells to CD86$^+$ cells of the TSA/Ag-PC-ZnO+IL-4 sample (≈1.8) was higher than that of the IL-4 sample (≈1.7) (Figure 5D,E).

Moreover, the effect of ipPZCHs to the expression of representative cytokines (interleukin-1β (IL-1β) and interleukin-10 (IL-10)) by RAW264.7 cells was also studied by enzyme-linked immunosorbent assay (ELISA) using the 10× degradation products of the composite hydrogels.[44,60,64] As shown in Figure 5F, the expression levels of IL-1β in SA/ZnO (114.1 ± 3.83 pg mL^{-1}), TSA/ZnO (110.8 ± 2.35 pg mL^{-1}), TSA/PC-ZnO (80.4 ± 5.84 pg mL^{-1}) and TSA/Ag-PC-ZnO (83.0 ± 7.32 pg mL^{-1}) groups were all lower than that of the control (127.7 ± 4.05 pg mL^{-1}) group, with the expression levels of the TSA/PC-ZnO and TSA/Ag-PC-ZnO samples the lowest ($p < 0.01$). The expression levels of IL-10 in all the composite hydrogel groups were also significantly ($p < 0.01$) higher than that of the control group, and the IL-10 expression levels in the TSA/PC-ZnO (415.5 ± 14.86 pg mL^{-1}) and TSA/Ag-PC-ZnO (405.5 ± 6.05 pg mL^{-1}) groups were significantly ($p < 0.05$) higher than that of the SA/ZnO and TSA/ZnO groups (Figure 5G). These results further confirm the immunomodulatory activity of ipPZCHs in downregulating the expression of proinflammatory cytokines and upregulating the expression of anti-inflammatory cytokines from macrophages.

All the above results prove that ipPZCHs exhibit favorable immunomodulatory activity to promote the M2 polarization of macrophages derived from the released Zn^{2+}, and PC-coordination tremendously accelerates Zn^{2+} release from PC-coordinated ZnOs, which assisted with the strong antioxidant activity of PC, further improves the immunomodulatory activity of TSA/PC-ZnO and TSA/Ag-PC-ZnO, and enhances the expression of anti-inflammatory cytokines from macrophages. The favorable immunomodulatory activity of ipPZCHs is beneficial for the osteogenesis during infected bone repair.

Furthermore, the in vitro osteogenic properties of ipPZCHs were assessed by investigating the effect of the degradation products of ipPZCHs to the osteogenic differentiation of rBMSCs, the following mineralization and the expression of representative osteogenic proteins. It can be seen from **Figure 6**A,B that the alkaline phosphatase (ALP) activities of the rBMSCs grown in osteogenic medium for all the composite hydrogel groups were significantly enhanced compared to that of the control group, especially on day 14. And the ALP activities of TSA/PC-ZnO (50.2 ± 0.88 U μg^{-1} protein) and TSA/Ag-PC-ZnO (45.1 ± 2.50 U μg^{-1} protein) groups on day 14 were also significantly higher than that of SA/ZnO (39.0 ± 2.25 U μg^{-1} protein) and TSA/ZnO (37.3 ± 2.41 U μg^{-1} protein) groups (Figure 6A,B), which might be attributed to the fast Zn^{2+} release from PC-coordinated ZnOs and help of the synchronously released antioxidative PC molecules. Obviously improved mineralization for the composite hydrogel groups was also observed from the alizarin red staining images (Figure 6C), especially for TSA/PC-ZnO and TSA/Ag-PC-ZnO groups and in the later stage on day 21. Western blotting results (Figure 6D and Figure S15, Supporting Information) show that the expression levels of collagen I (COL-1) and osteopontin (OPN) of the SA/ZnO group were slightly lower than that of the control group, but the TSA/ZnO group showed a mild upregulation in the expression of COL-1, Runt-related transcription factor 2 (Runx2) and OPN comparing to the control group. The expression levels of COL-1, Runx2 and OPN in the TSA/PC-ZnO and TSA/Ag-PC-ZnO groups were all significantly higher than that of the SA/ZnO group. The expression levels of OPN in the TSA/PC-ZnO and TSA/Ag-PC-ZnO groups exhibited the highest increase, nearly twice the level of the control group (Figure 6D and Figure S15, Supporting Information). These results preliminarily prove the favorable osteogenic properties of ipPZCHs, especially for the composite hydrogels with PC-coordinated ZnOs, which is deemed derived from the accelerated Zn^{2+} release and the scavenge of possible excess exogenous ROS (produced by ZnO) by strongly antioxidant PC. It is also confirmed that the inclusion of Ag NPs did not significantly affect the osteogenic properties of ipPZCHs, beneficial for the practical application of ipPZCHs in infected bone repair.

2.6. In Vivo Study

To further investigate the antimicrobial activity of ipPZCHs, an in vivo antibacterial experiment was also conducted using a femoral condyle infection model created on Sprague Dawley (SD) rats by injection of *S. aureus* and allowed bacterial infection for 10 d before debriding and implanting composite hydrogel (Figure S16A, Supporting Information). As shown in Figure S16B,C in the Supporting Information, after 72 h treatment, the amounts of the bacteria survival ratios of the composite hydrogel groups were all < 75%, and the bacterial survival ratios of the TSA/PC-ZnO (21.7% ± 3.35%) and TSA/Ag-PC-ZnO (11.4% ± 2.64%) groups were significantly ($p < 0.01$) lower than that of the SA/ZnO (71.3% ± 2.06%) and TSA/ZnO (64.2% ± 3.74%) groups. These results confirm the favorable in vivo antimicrobial activity of ipPZCHs due to that thioether introduction in TSA induces ROS-responsibility, PC-coordination in the modified ZnOs increases Zn^{2+} releasing rates, and the application of Ag-Zn dual metal antimicrobial mechanism.

To further evaluate the infected bone repair efficacy of ipPZCHs, the representative composite hydrogels (SA/ZnO, TSA/ZnO, TSA/PC-ZnO, and TSA/Ag-PC-ZnO) were injected into the defect sites of an infected femoral condylar bone defect model on SD rats following debridement, and their effect to bone regeneration was assessed via micro-computed tomography (micro-CT), histological, immunohistochemical and immunofluorescence staining 4, 8, and 12 weeks after operation. A blank control with the defected untreated was set for comparison. As shown in Figure 6E, big and empty bone cavities still could be observed from the reconstructed sagittal and coronal 2D images and 3D images of the treated bone defects at week 4 post operation, especially for the control and SA/ZnO groups. Both bone mineral densities (BMDs) and bone volume/tissue volume values (BV/TVs) for all samples increased with time prolongation (Figure 6F,G), the cortical bone defects were nearly sealed after 12 weeks except for the control and SA/ZnO samples (Figure 6E). The bone regeneration rates of the TSA/ZnO, TSA/PC-ZnO and TSA/Ag-PC-ZnO groups were significantly higher than that of the control and SA/ZnO groups, with both BMDs and BV/TVs of all the former three groups significantly higher than that of the latter two groups for all the three time-points (Figure 6E–G). This is believed can be attributed to that the favorable ROS-responsibility of TSA containing composite hydrogels well adapted the high ROS microenvironment of the infected bone defects, to accelerate the release of ZnO or PC-coordinated ZnOs and promote bone regeneration. Although the TSA/PC-ZnO and TSA/Ag-PC-ZnO groups showed only slightly higher BMDs and BV/TVs than that of the TSA/ZnO group especially at later stage (Figure 6F,G), the reconstructed CT images confirmed that the former two groups induced faster and better cortical bone closure comparing to the latter one (Figure 6E). This can also be confirmed from the hematoxylin and eosin (H & E) (Figure S17, Supporting Information) and Masson's trichrome (Figure 6H) staining images, in which obvious tissue cavities can be seen in the control, SA/ZnO and TSA/ZnO groups but not in the TSA/PC-ZnO and TSA/Ag-PC-ZnO groups at week 4 and 8. Some new tissue but mostly fibrous tissue could be observed in the control group at week 12, indicating delayed bone healing caused by the infected microenvironment. The collagen deposition contents of the control and SA/ZnO groups showed no significant difference ($p > 0.05$) at week 4 and 8 (Figure 6I), well agreeing with the micro-CT results (Figure 6E–G). At week 12, the collagen deposition content of the SA/ZnO group (21.1% ± 2.68%) was even lower than that of the control group (28.2%

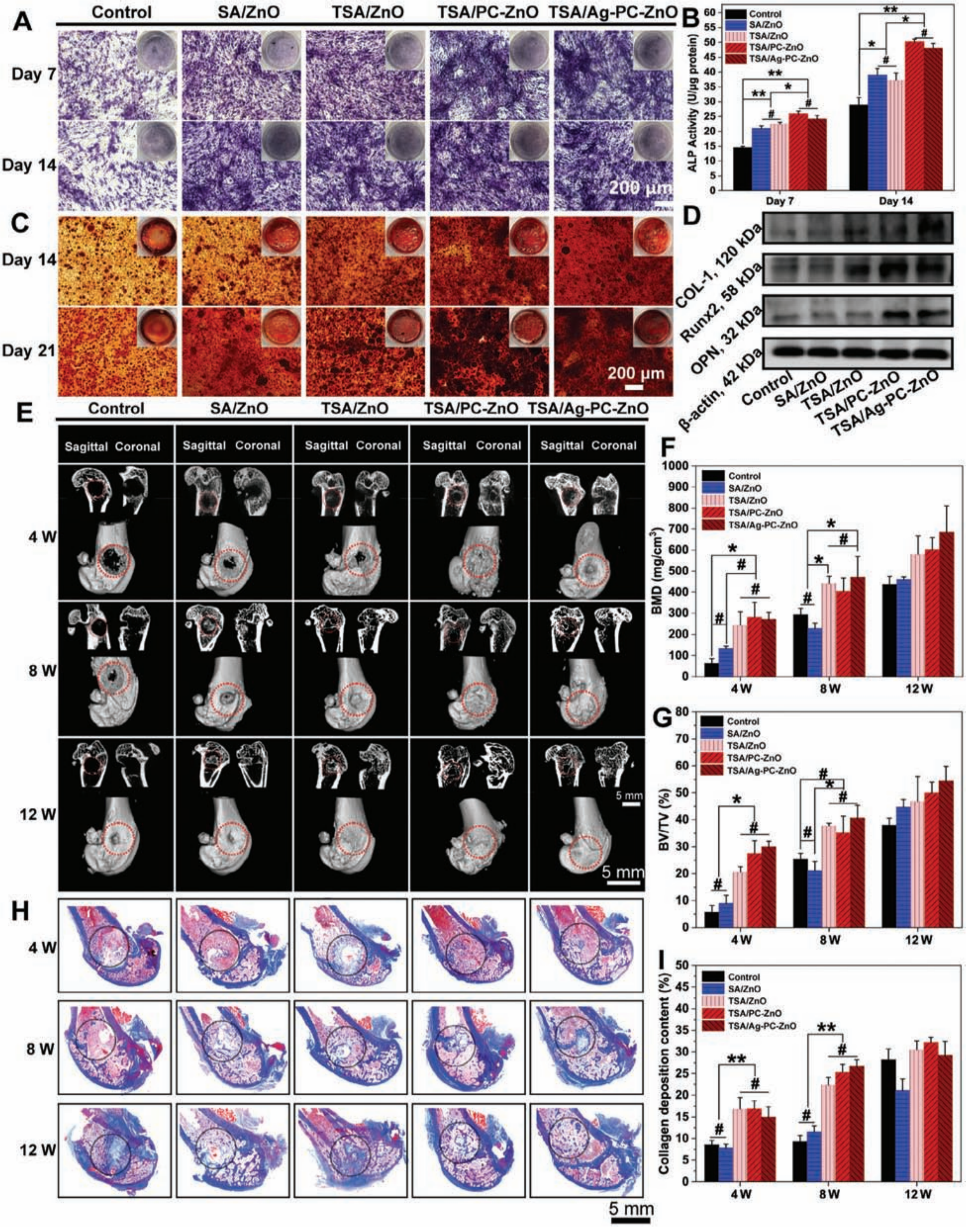

Figure 6. In vivo osteogenic performance of ipPZCHs: A) ALP staining images and B) the quantitative ALP activities of rBMSCs treated by the degradation products of composite hydrogels, C) alizarin red staining images, and D) the expression levels of osteogenic related proteins (COL-1, Runx2, and OPN) on day 7 ($n = 3$). E) The 2D (sagittal and coronal) and 3D reconstructed micro-CT images of the treated femurs at week 4, 8, and 12, and the calculated F) bone mineral density (BMD) and G) bone volume/tissue volume (BV/TV) results. H) Representative Masson's trichrome staining images and I) the collagen deposition contents of different groups at week 4, 8, and 12 ($n = 3$). $^{*}p < 0.05$, $^{**}p < 0.01$, $^{\#}$ represents no significant difference ($p > 0.05$).

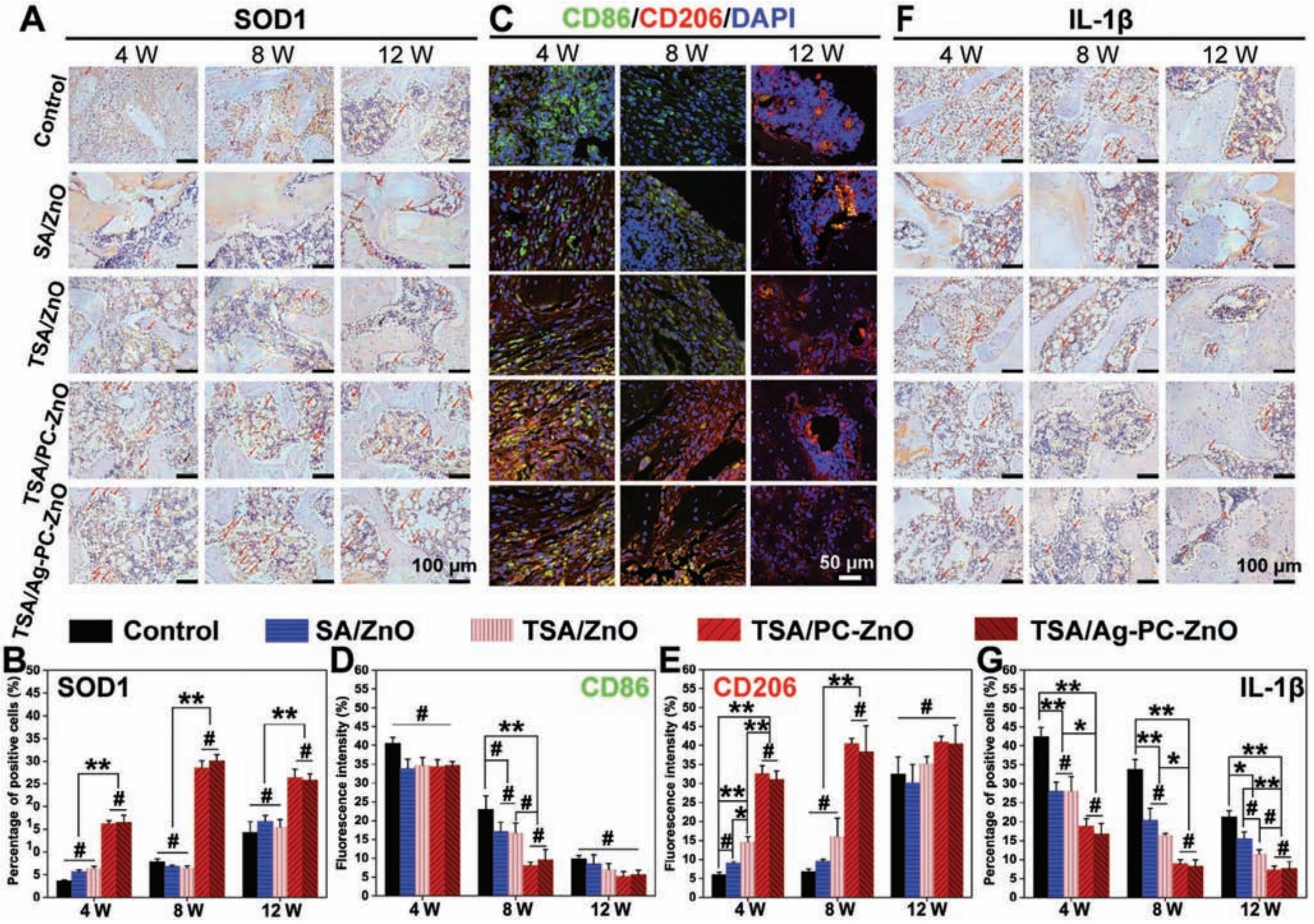

Figure 7. In vivo antioxidant, immunomodulatory, and anti-inflammatory assessment of ipPZCHs: A) superoxide dismutase I (SOD1) immunohistochemical staining images and B) the percentages of SOD1 positive cells for different groups at week 4, 8, and 12. C) CD86 (M1) and CD206 (M2) immunofluorescence colocation images and the calculated fluorescence intensities (% Area) of D) CD86 and E) CD206 for different groups at week 4, 8, and 12. F) interleukin-1β (IL-1β) immunohistochemical staining images and G) the percentages of IL-1β^+ cells for different groups at week 4, 8, and 12. (The red arrow indicates positive cells.) $*p < 0.05$, $**p < 0.01$, $^{\#}$ represents no significant difference, $n = 3$ ($p > 0.05$) μm.

± 2.48%), which might be attributed to that the slow degradation of SA/ZnO obstructed bone regeneration and more fibrous tissue grew in the control group (Figure 6H,I). All the TSA containing composite hydrogel groups induced significantly higher collagen deposition than the control and SA/ZnO groups for all the three time-points, but there were no significant differences between the TSA/ZnO, TSA/PC-ZnO and TSA/Ag-PC-ZnO groups (Figure 6I). The formed new bone tissue for the TSA/ZnO, TSA/PC-ZnO and TSA/Ag-PC-ZnO groups almost filled the defect areas and exhibited morphological characteristics similar to autologous bone trabeculae at week 8 and 12, suggesting the favorable osteogenic properties of ipPZCHs, and the importance of the introduction of ROS-responsibility to accelerate hydrogels' degradation and vacate space for bone in-growth. Effective infection control by ipPZCHs at an early stage (Figure S16, Supporting Information), due to ROS-responsible hydrogel disintegration, PC-coordination resultant fast release of antimicrobial metal ions (Zn^{2+} and Ag^+) and the application of Ag-Zn dual metal antimicrobial mechanism, is also beneficial for the long-term osteogenesis.

Excessive inflammatory reactions can prevent osteogenesis, ultimately leading to delayed bone healing or even implantation failure. Therefore, the in vivo antioxidant and immunomodulatory properties of ipPZCHs were assessed by immunohistochemical staining of SOD1 and IL-1β, as well as immunofluorescence staining of macrophages with CD86 as the M1 surface marker and CD206 as the M2 surface marker. As shown in **Figure 7**A,B, at all the three tested time-points, the SOD1 expression levels of the SA/ZnO and TSA/ZnO groups showed no significant difference ($p > 0.05$) to that of the control group, and they were all significantly lower ($p < 0.01$) than the SOD1 expression levels of the TSA/PC-ZnO and TSA/Ag-PC-ZnO groups, well agreeing with the in vitro antioxidant ability results (Figure 2G). The rouse of the endogenous antioxidant system in vivo further enhances the antioxidant activity of TSA/PC-ZnO and TSA/Ag-PC-ZnO, beneficial to enhance cellular resistance to the high ROS microenvironment and facilitate immune cells to exert their immunomodulatory effect. The representative CD86 (green color) and CD206 (red color) immunofluorescence colocalization images and the corresponding quantitative results (Figure 7C–E) of the treated

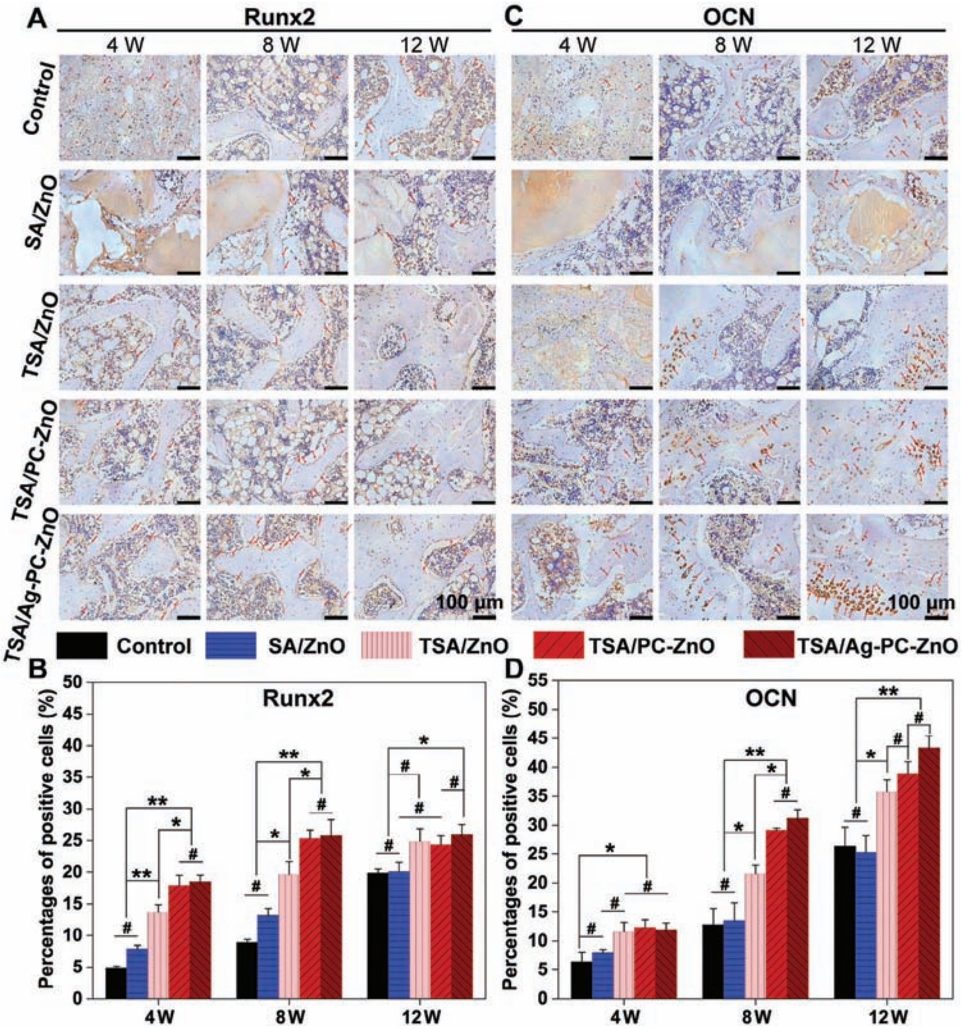

Figure 8. Immunohistochemical staining results of osteogenic proteins: immunohistochemical staining images of A) Runt-related transcription factor 2 (Runx2) and C) osteocalcin (OCN) as well as the calculated percentages of positive cells for B) Runx2 and D) OCN at week 4, 8, and 12. (The red arrow indicates positive cells.) $*p < 0.05$, $**p < 0.01$, $^{\#}$ represents no significant difference, $n = 3$ ($p > 0.05$).

bone defects show that at week 4, the macrophages in all groups were predominantly in proinflammatory (M1) phenotype, but the amounts of $CD86^+$ cells of all the composite hydrogel groups was lower than the control group. A mild immune response is essential to combat bacterial infection and recruit mesenchymal stem cells (MSCs) for osteogenesis. The immune response gradually faded with time, and the fading speeds of TSA/PC-ZnO and TSA/Ag-PC-ZnO were significantly faster than that of the control, SA/ZnO and TSA/ZnO groups (Figure 7D), suggesting the favorable anti-inflammatory properties of ipPZCHs. Moreover, the numbers of M2-type macrophages of all the TSA-containing composite groups, especially TSA/PC-ZnO and TSA/Ag-PC-ZnO groups, were all significantly higher than that of the control and SA/ZnO group at week 4 and 8 (Figure 7E), further confirming the strong anti-inflammatory properties of ipPZCHs. The expression levels of IL-1β, a key mediator of the inflammatory response, in all the composite hydrogel groups were also significantly ($p < 0.05$) lower than that of the control group at all the three time-points (Figure 7F,G). And the IL-1β expression levels for the TSA/PC-ZnO and TSA/Ag-PC-ZnO groups were also significantly ($p < 0.05$) lower than that of the SA/ZnO and TSA/ZnO groups at week 4 and 8. At week 12, the IL-1β expression levels of all the TSA-containing composite hydrogel groups were no longer significantly different from each other, but still slightly lower than that of the SA/ZnO and control groups (Figure 7G). It is deemed that the ROS-responsive release of antimicrobial components from ipPZCHs in the infected bone defect sites, and PC-Zn^{2+} coordination induced fast release of antimicrobial metal ions augmented bacterial killing in the early stage. This, together with the synchronously released antioxidant PC molecules, accelerated the fading of immune response and promoted the M2 polarization of macrophages favorable for osteogenesis.

To further study the effect of ipPZCHs to osteogenesis during infected bone repair, Runx2 and OCN were selected as the representative markers for the early and later stage of osteogenic differentiation respectively and investigated by immunohistochemical staining. As shown in **Figure 8**A,B, at week 4 and 8, the Runx2 expression levels of all the TSA-containing composite hydrogel groups were significantly higher than the other groups, and the Runx2 expression levels of the TSA/PC-ZnO and TSA/Ag-PC-ZnO groups were also higher than that of the TSA/ZnO group, indicating that both ROS-responsible release of modified/unmodified ZnOs and PC-Zn^{2+} coordination induced fast Zn^{2+} release promoted osteogenic differentiation of MSCs. Although the Runx2 expression levels of the TSA-containing composite hydrogel groups were still significantly higher than the control and SA/ZnO groups at week 12, the differences between them became smaller, implying the mature of osteoblasts and delayed osteogenesis for the control and SA/ZnO groups (Figure 8A,B). This can be further confirmed by the OCN immunohistochemical staining results (Figure 8C,D), in which differences between the OCN expression levels of the TSA-containing composite hydrogel groups and the other groups became significant after 8 weeks. And the OCN expression levels of the TSA/PC-ZnO and TSA/Ag-PC-ZnO groups were also significantly higher than that of the TSA/ZnO group, once more confirming the important role of PC-Zn^{2+} coordination induced fast Zn^{2+} release on the promotion of osteogenic properties (Figure 8C,D). The slow degradation of SA/ZnO led to a "volume occupation" effect, might be one of the reasons of the delayed osteogenesis for the SA/ZnO group, once more proving the importance of the application of ROS-responsible degradation strategy in ipPZCHs from the reverse side.

Although no significant difference in new bone growth was found between the TSA/ZnO, TSA/PC-ZnO, and TSA/Ag-PC-ZnO groups at the micro-CT level, the histological, immunohistochemical, and immunofluorescence staining results confirmed the superior antioxidant and immunomodulatory activity as well as enhanced osteogenic properties of the TSA/PC-ZnO and TSA/Ag-PC-ZnO groups comparing to the TSA/ZnO group. It is believed that the slow degradation of ZnO in the TSA/ZnO group might contribute to the high BMD and BV/TV values, given that ZnO particles are also visible in micro-CT.

3. Conclusion

In summary, by simply compositing reactive oxygen species (ROS)-responsive TSA with PC-coordinated zinc oxide (ZnO) microspheres followed by calcium chloride ($CaCl_2$) crosslinking, injective programmable proanthocyanidin-coordinated zinc-based composite hydrogels (ipPZCHs) are developed for accelerating infected bone repair. Thioether introduction in TSA confers ipPZCHs with favorable ROS-responsibility to quickly disintegrate in the high-ROS microenvironment of infected bone defect sites, and PC-Zn^{2+} coordination further accelerates the release of Zn^{2+} and Ag^+ to combat bacterial infection, the exogenous ROS produced during antimicrobial process further speeds up the disintegration of ipPZCH hydrogel thus augments the antimicrobial capability. At the same time, ROS-responsive degradation of ipPZCHs vacates space for bone ingrowth. The synchronously released PC molecules provide strong antioxidant activity, sufficiently scavenges excess ROS, thus enhances the immunomodulatory activity of Zn^{2+} by promoting the anti-inflammatory phenotype (M2) polarization of macrophages, and improves the osteoinductive properties of Zn^{2+}, to promote osteogenesis and facilitate infected bone repair. Smartly leveraging, being able to response to and change the high ROS microenvironment of the infected bone defects, to amplify the antimicrobial performance and self-adaptively scavenge excess ROS thus promote the sequential osteogenesis, the developed ipPZCHs have a great application potential in infected bone repair. This design strategy can also be universally expanded to other complicated tissue engineering scenarios and inspire more innovations in smart biomaterials and self-adaptive regenerative medicines.

4. Experimental Section

Material Preparation: PC-coordinated ZnO (PC-ZnO) and Ag NPs modified and PC-coordinated ZnO (Ag-PC-ZnO) were synthesized via a hydrothermal reaction method adapted from the synthesis method of pure ZnO by adding PC or PC and $AgNO_3$ in the system. ROS-responsive thioether grafted sodium alginate (TSA) was synthesized by reacting sodium alginate (SA) with 2-(methylthio) ethanol (ME) in the presence of 1-ethyl-(3-dimethylaminopropyl) carbodiimide hydrochloride (EDC·HCl). The composite hydrogels were prepared by crosslinking the suspending solution of ZnO or modified ZnOs in SA/TSA solution (solution A) with $CaCl_2$ solution (solution B).

Characterizations: ZnO and modified ZnOs were characterized by ATR-FTIR, XRD, TGA, and SEM. The successful synthesis of TSA was determined by ^{1}H-NMR and FTIR. And the metal ions and PC release performance of ZnO, modified ZnOs and the composite hydrogels was investigated by ICP-MS and UV–vis spectrometer. The mechanical property of the composite hydrogels was characterized using a universal material testing machine (Instron 34TM-10), and the swelling, degradation profiles of the composite hydrogels were also studied.

In Vitro Studies: The in vitro antioxidant activity of the modified ZnO and composite hydrogels was assessed by DPPH assay, H_2O_2 scavenging assay, intracellular ROS scavenging tests and intracellular activities tests of SOD, CAT, and GPx. The antimicrobial ability of the composite hydrogels was assessed by measuring the minimal inhibitory concentrations (MICs) of modified/unmodified ZnO and testing the antibacterial kinetics of the composite hydrogels against *S. aureus* and *E. coli*. Co-culture of *E. coli* and rBMSCs together with the ipPZCH composite hydrogel was also conducted to study the tissue protection ability of the hydrogel by killing bacteria and scavenging ROS. The cytocompatibility of ZnO and modified ZnOs was assessed by measuring the cell viabilities at different concentrations using rBMSC and RAW264.7 as cell models, and investigating the effect of ZnO and modified ZnOs to the mitochondrial membrane potential ($\Delta\psi m$) with JC-1 kit against RAW264.7. The cytocompatibility of the composite hydrogels was assessed by evaluating the cytotoxicity of sol contents and degradation products of the composite hydrogels. The immunomodulatory ability of the composite hydrogels was assessed by flow cytometry and immunofluorescence staining, as well as by determining the expression of IL-1β and IL-10 by RAW264.7 cells via ELISA. The in vitro osteogenic properties of the composite hydrogels were assessed by investigating the effect of the composite hydrogels′ degradation products to the osteogenic differentiation of rBMSCs via ALP activity test, alizarin red staining and Western blotting of representative osteogenic proteins (Runx2, OPN, and COL-1).

In Vivo Experiments: All animal experiments were conducted in compliance with the Animal Experimental Committee of Institute of Biological and Medical Engineering, Guangdong Academy of Sciences (Approval No. 2021013). The infected femoral condyle defect model was created on SD rats and the composite hydrogels were injected, the in vivo antibacterial activity was assessed 3 d after the operation, and micro-CT analysis and histological examination were also conducted 4, 8, and 12 weeks post operation. H & E, Masson's trichrome staining, immunofluorescence staining (CD86 and CD206), and immunohistochemical staining (IL-1β, Runx2 and OCN) were conducted to the assess the osteogenic, in vivo antioxidant and immunomodulatory properties of the composite hydrogels.

The detailed experimental processes are described in the Supporting Information.

Supporting Information

Supporting Information is available from the Wiley Online Library or from the author.

Acknowledgements

Y.W. and Y.Z. contributed equally to this work. This work was supported by the Natural Science Foundation of China (Grant Nos. U21A2099, 82272453, and 82102545), the Youth Talent of Guangdong Special Support Program (0620220207), the Basic and Applied Basic Research Project of Guangzhou City (202201011774), and the Open Program from Guangdong Provincial Key Laboratory of Bone and Joint Degeneration Disease.

Conflict of Interest

The authors declare no conflict of interest.

Data Availability Statement

The data that support the findings of this study are available from the corresponding author upon reasonable request.

Keywords

infected bone defects, proanthocyanidin, ROS-responsiveness, silver, zinc oxide

Received: August 16, 2023
Revised: October 22, 2023
Published online: November 13, 2023

---

[1] C. T. Johnson, J. A. Wroe, R. Agarwal, K. E. Martin, R. E. Guldberg, R. M. Donlan, L. F. Westblade, A. J. Garcia, *Proc. Natl. Acad. Sci. U. S. A.* **2018**, *115*, E4960.
[2] M. Rupp, D. Popp, V. Alt, *Injury* **2020**, *51*, S57.
[3] E. A. Masters, R. P. Trombetta, K. L. De Mesy Bentley, B. F. Boyce, A. L. Gill, S. R. Gill, K. Nishitani, M. Ishikawa, Y. Morita, H. Ito, S. N. Bello-Irizarry, M. Ninomiya, J. D. Brodell, C. C. Lee, S. P. Hao, I. Oh, C. Xie, H. A. Awad, J. L. Daiss, J. R. Owen, S. L. Kates, E. M. Schwarz, G. Muthukrishnan, *Bone Res.* **2019**, *7*, 20.
[4] X. Jin, Y.-H. Xiong, X.-Y. Zhang, R. Wang, Y. Xing, S. Duan, D. Chen, W. Tian, F.-J. Xu, *Adv. Funct. Mater.* **2019**, *29*, 1807915.
[5] Z. Yuan, J. Wu, Z. Fu, S. Meng, L. Dai, K. Cai, *Adv. Funct. Mater.* **2022**, *32*, 2200374.
[6] C. T. Johnson, M. C. P. Sok, K. E. Martin, P. P. Kalelkar, J. D. Caplin, E. A. Botchwey, A. J. García, *Sci. Adv.* **2019**, *5*, eaaw1228.
[7] D. Yang, A. R. Wijenayaka, L. B. Solomon, S. M. Pederson, D. M. Findlay, S. P. Kidd, G. J. Atkins, *mBio* **2018**, *9*, e00415.
[8] B. Fang, P. Qiu, C. Xia, D. Cai, C. Zhao, Y. Chen, H. Wang, S. Liu, H. Cheng, Z. Tang, B. Wang, S. Fan, X. Lin, *Biomaterials* **2021**, *268*, 120603.
[9] Y. Zhao, X. Peng, D. Wang, H. Zhang, Q. Xin, M. Wu, X. Xu, F. Sun, Z. Xing, L. Wang, P. Yu, J. Xie, J. Li, H. Tan, C. Ding, J. Li, *Adv. Sci.* **2022**, *9*, 2204535.
[10] Y. Zhang, J. Zhou, J.-L. Wu, J.-C. Ma, H. Wang, J. Wen, S. Huang, M. Lee, X. Bai, Z.-K. Cui, *J. Controlled Release* **2023**, *354*, 713.
[11] L. Schnaider, S. Brahmachari, N. W. Schmidt, B. Mensa, S. Shaham-Niv, D. Bychenko, L. Adler-Abramovich, L. J. W. Shimon, S. Kolusheva, W. F. Degrado, E. Gazit, *Nat. Commun.* **2017**, *8*, 1365.
[12] K. Chae, W. Y. Jang, K. Park, J. Lee, H. Kim, K. Lee, C. K. Lee, Y. Lee, S. H. Lee, J. Seo, *Sci. Adv.* **2020**, *6*, eabb0025.
[13] Y. Li, Y. Miao, L. Yang, Y. Zhao, K. Wu, Z. Lu, Z. Hu, J. Guo, *Adv. Sci.* **2022**, *9*, 2202684.
[14] S. Hussain, J. Joo, J. Kang, B. Kim, G. B. Braun, Z.-G. She, D. Kim, A. P. Mann, T. Mölder, T. Teesalu, S. Carnazza, S. Guglielmino, M. J. Sailor, E. Ruoslahti, *Nat. Biomed. Eng.* **2018**, *2*, 95.
[15] Y. Li, Y. Miao, L. Yang, G. Wang, M. Fu, Y. Wang, D. Fu, J. Huang, J. Wang, Z. Fan, Z. Lu, J. Guo, Z. Hu, *Chem. Eng. J.* **2023**, *455*, 140572.
[16] Y. Zhao, J. Li, L. Liu, Y. Wang, Y. Ju, C. Zeng, Z. Lu, D. Xie, J. Guo, *Adv. Healthcare Mater.* **2023**, *12*, 2300303.
[17] P. P. Kalelkar, M. Riddick, A. J. García, *Nat. Rev. Mater.* **2022**, *7*, 39.
[18] Y. Ding, X. Hu, Y. Piao, R. Huang, L. Xie, X. Yan, H. Sun, Y. Li, L. Shi, Y. Liu, *ACS Nano* **2023**, *17*, 6601.
[19] M. Fu, Y. Zhao, Y. Wang, Y. Li, M. Wu, Q. Liu, Z. Hou, Z. Lu, K. Wu, J. Guo, *Small* **2023**, *19*, e2205489.
[20] I. Zhuk, F. Jariwala, A. B. Attygalle, Y. Wu, M. R. Libera, S. A. Sukhishvili, *ACS Nano* **2014**, *8*, 7733.
[21] D. Hu, Y. Deng, F. Jia, Q. Jin, J. Ji, *ACS Nano* **2020**, *14*, 347.
[22] L. Su, Y. Li, S. Tian, F. Huang, Y. Ren, C. Yang, H. C. Van Der Mei, H. J. Busscher, L. Shi, *Acta Biomater.* **2022**, *154*, 559.
[23] W. Xiu, S. Gan, Q. Wen, Q. Qiu, S. Dai, H. Dong, Q. Li, L. Yuwen, L. Weng, Z. Teng, Y. Mou, L. Wang, *Research* **2020**, *2020*, 9426453.
[24] Y. Zhan, X. Hu, Y. Li, Y. Wang, H. Chen, C. A. Omolo, T. Govender, H. Li, F. Huang, L. Shi, X. Hu, Y. Liu, *Adv. Funct. Mater.* **2023**, *33*, 2214299.
[25] Y. Hu, X. Ruan, X. Lv, Y. Xu, W. Wang, Y. Cai, M. Ding, H. Dong, J. Shao, D. Yang, X. Dong, *Nano Today* **2022**, *46*, 101602.
[26] J. Li, Z. Ding, Y. Li, J. Miao, W. Wang, K. Nundlall, S. Chen, *Mater. Des.* **2020**, *195*, 109021.
[27] S. Liu, Q. Zhang, J. Yu, N. Shao, H. Lu, J. Guo, X. Qiu, D. Zhou, Y. Huang, *Adv. Healthcare Mater.* **2020**, *9*, e2000198.
[28] A. Wang, S. Duan, X. Ding, N. Zhao, Y. Hu, X. Ding, F.-J. Xu, *Adv. Funct. Mater.* **2021**, *31*, 2011165.
[29] Y. Liu, H. J. Busscher, B. Zhao, Y. Li, Z. Zhang, H. C. Van Der Mei, Y. Ren, L. Shi, *ACS Nano* **2016**, *10*, 4779.
[30] K. Wu, M. Fu, Y. Zhao, E. Gerhard, Y. Li, J. Yang, J. Guo, *Bioact. Mater.* **2023**, *20*, 93.
[31] T. Cui, S. Wu, Y. Sun, J. Ren, X. Qu, *Nano Lett.* **2020**, *20*, 7350.
[32] Y. Li, X. Liu, B. Li, Y. Zheng, Y. Han, D.-F. Chen, K. W. K. Yeung, Z. Cui, Y. Liang, Z. Li, S. Zhu, X. Wang, S. Wu, *ACS Nano* **2020**, *14*, 8157.
[33] T. Kim, Q. Zhang, J. Li, L. Zhang, J. V. Jokerst, *ACS Nano* **2018**, *12*, 5615.
[34] Y. Wang, Y. Yang, Y. Shi, H. Song, C. Yu, *Adv. Mater.* **2020**, *32*, 1904106.
[35] A. El-Fiqi, N. Mandakhbayar, S. B. Jo, J. C. Knowles, J. H. Lee, H. W. Kim, *Bioact. Mater.* **2021**, *6*, 123.
[36] K. Gold, B. Slay, M. Knackstedt, A. K. Gaharwar, *Adv. Ther.* **2018**, *1*, 1700033.
[37] J. Guo, X. Tian, D. Xie, K. Rahn, E. Gerhard, M. L. Kuzma, D. Zhou, C. Dong, X. Bai, Z. Lu, J. Yang, *Adv. Funct. Mater.* **2020**, *30*, 2002438.
[38] X. Qu, H. Yang, B. Jia, Z. Yu, Y. Zheng, K. Dai, *Acta Biomater.* **2020**, *117*, 400.
[39] W. Guan, L. Tan, X. Liu, Z. Cui, Y. Zheng, K. W. K. Yeung, D. Zheng, Y. Liang, Z. Li, S. Zhu, X. Wang, S. Wu, *Adv. Mater.* **2021**, *33*, 2006047.
[40] X. Qu, H. Yang, Z. Yu, B. Jia, H. Qiao, Y. Zheng, K. Dai, *Bioact. Mater.* **2020**, *5*, 410.
[41] X. Fu, Y. Li, T. Huang, Z. Yu, K. Ma, M. Yang, Q. Liu, H. Pan, H. Wang, J. Wang, M. Guan, *Adv. Sci.* **2018**, *5*, 1700755.
[42] H. Yang, B. Jia, Z. Zhang, X. Qu, G. Li, W. Lin, D. Zhu, K. Dai, Y. Zheng, *Nat. Commun.* **2020**, *11*, 401.
[43] B. Yeom, T. Sain, N. Lacevic, D. Bukharina, S.-H. Cha, A. M. Waas, E. M. Arruda, N. A. Kotov, *Nature* **2017**, *543*, 95.
[44] W. Liu, J. Li, M. Cheng, Q. Wang, K. W. K. Yeung, P. K. Chu, X. Zhang, *Adv. Sci.* **2018**, *5*, 1800749.

[45] Y.-W. Wang, A. Cao, Y. Jiang, X. Zhang, J.-H. Liu, Y. Liu, H. Wang, *ACS Appl. Mater. Interfaces* **2014**, *6*, 2791.

[46] G. Applerot, A. Lipovsky, R. Dror, N. Perkas, Y. Nitzan, R. Lubart, A. Gedanken, *Adv. Funct. Mater.* **2009**, *19*, 842.

[47] A. Rauf, M. Imran, T. Abu-Izneid, Iahtisham-Ul-Haq, S. Patel, X. Pan, S. Naz, A. Sanches Silva, F. Saeed, H. A. Rasul Suleria, *Biomed. Pharmacother.* **2019**, *116*, 108999.

[48] R. Liu, B. Zhou, H. Zhang, Y. Chen, C. Fan, T. Zhang, T. Qin, J. Han, S. Zhang, X. Chen, W. Shen, J. Chang, Z. Yin, *Chem. Eng. J.* **2021**, *420*, 129415.

[49] Z. Wu, Q. Hou, T. Chen, X. Jiang, L. Wang, J. Xu, L. Wang, *Biomaterials* **2022**, *291*, 121900.

[50] J. Guo, T. Suma, J. J. Richardson, H. Ejima, *ACS Biomater. Sci. Eng.* **2019**, *5*, 5578.

[51] V. B. Maisuria, M. Okshevsky, E. Déziel, N. Tufenkji, *Adv. Sci.* **2022**, *9*, e2202641.

[52] Z. Lu, J. Zhou, A. Wang, N. Wang, X. Yang, *J. Mater. Chem.* **2011**, *21*, 4161.

[53] W. Shi, S. Song, H. Zhang, *Chem. Soc. Rev.* **2013**, *42*, 5714.

[54] Y. Guo, Q. Sun, F.-G. Wu, Y. Dai, X. Chen, *Adv. Mater.* **2021**, *33*, 2007356.

[55] J. Wei, Y. Liang, Y. Hu, B. Kong, J. Zhang, Q. Gu, Y. Tong, X. Wang, S. P. Jiang, H. Wang, *Angew. Chem., Int. Ed.* **2016**, *55*, 12470.

[56] G. Lin, J. J. Richardson, H. Ahmed, Q. A. Besford, A. J. Christofferson, S. Beyer, Z. Lin, A. R. Rezk, M. Savioli, J. Zhou, C. F. Mcconville, C. Cortez-Jugo, L. Y. Yeo, F. Caruso, *Adv. Mater.* **2021**, *33*, 2006177.

[57] Z. Jia, P. Xiu, M. Li, X. Xu, Y. Shi, Y. Cheng, S. Wei, Y. Zheng, T. Xi, H. Cai, Z. Liu, *Biomaterials* **2016**, *75*, 203.

[58] T. Liu, B. Xiao, F. Xiang, J. Tan, Z. Chen, X. Zhang, C. Wu, Z. Mao, G. Luo, X. Chen, J. Deng, *Nat. Commun.* **2020**, *11*, 2788.

[59] A. Lueckgen, D. S. Garske, A. Ellinghaus, R. M. Desai, A. G. Stafford, D. J. Mooney, G. N. Duda, A. Cipitria, *Biomaterials* **2018**, *181*, 189.

[60] Q. Chen, J. Li, F. Han, Q. Meng, H. Wang, Q. Wei, Z. Li, F. Li, E. Xie, X. Qin, S. Chen, W. Wang, C. Liu, B. Li, F. Han, *Adv. Funct. Mater.* **2022**, *32*, 2201067.

[61] J. Li, F. Han, J. Ma, H. Wang, J. Pan, G. Yang, H. Zhao, J. Zhao, J. Liu, Z. Liu, B. Li, *Adv. Funct. Mater.* **2022**, *32*, 2111208.

[62] D. Li, K. Chen, H. Tang, S. Hu, L. Xin, X. Jing, Q. He, S. Wang, J. Song, L. Mei, R. D. Cannon, P. Ji, H. Wang, T. Chen, *Adv. Mater.* **2022**, *34*, 2108430.

[63] H. Liu, Y. Du, J.-P. St-Pierre, M. S. Bergholt, H. Autefage, J. Wang, M. Cai, G. Yang, M. M. Stevens, S. Zhang, *Sci. Adv.* **2020**, *6*, eaay7608.

[64] O. R. Mahon, D. C. Browe, T. Gonzalez-Fernandez, P. Pitacco, I. T. Whelan, S. Von Euw, C. Hobbs, V. Nicolosi, K. T. Cunningham, K. H. G. Mills, D. J. Kelly, A. Dunne, *Biomaterials* **2020**, *239*, 119833.